



Micro-scale pollution mechanism of dust diffusion in a blasting driving face based on CFD-DEM coupled model

Haiming Yu¹ · Weimin Cheng^{1,2} · Yao Xie¹ · Huitian Peng¹

Received: 27 January 2018 / Accepted: 9 April 2018 / Published online: 23 May 2018
© Springer-Verlag GmbH Germany, part of Springer Nature 2018

Abstract

In order to investigate the diffuse pollution mechanisms of high-concentration dusts in the blasting driving face, the airflow-dust coupled model was constructed based on CFD-DEM coupled model; the diffusion rules of the dusts with different diameters at microscopic scale were analyzed in combination with the field measured results. The simulation results demonstrate that single-exhaust ventilation exhibited more favorable dust suppression performance than single-forced ventilation. Under single-exhaust ventilation condition, the motion trajectories of the dusts with the diameter smaller than 20 μm were close to the airflow streamline and these dusts were mainly distributed near the footway walls; by contrast, under single-forced ventilation condition, the motion trajectories of the dust particles with a diameter range of 20–40 μm were close to the airflow streamlines, and a large number of dusts with the diameter smaller than 20 μm accumulated in the regions 5 m and 17–25 m away from the head-on section. Moreover, under the single-exhaust ventilation, the relationship between dust diameter D and negative-pressured-induced dust emission ratio P can be expressed as $P = -25.03\ln(D) + 110.39$, and the dust emission ratio was up to 74.36% for 7-μm dusts, and the path-dependent settling behaviors of the dusts mainly occurred around the head-on section; under single-forced ventilation condition, the z value of the dusts with the diameter over 20 μm decreased and the dusts with a diameter smaller than 7 μm are particularly harmful to human health, but their settling ratios were below 22.36%.

Keywords Blasting driving face · Dust particle size · CFD-DEM · Diffusion-induced pollution

Introduction

Besides oil and natural gas, coal is one of the indispensable energy sources for industrial production and human life. However, mine dusts are inevitably produced in coal mining and production, which would seriously pollute the working environment, reduce the visibility at production site, and greatly threaten the miners' physical and psychological health. According to the notification by the National Health and Family Planning Commission of PRC, the cumulative number

of occupational disease cases in China was as high as 863,634 by 2014, of which 777,173 were pneumoconiosis cases, accounting for 89.99% of the total occupational disease cases in China (Nie et al. 2012). In 2014, the workers in coal mining and some mining-supporting industries were at particularly high risks of pneumoconiosis, and they accounted for 94.21% of the newly added pneumoconiosis cases (Zhou et al. 2016a). Blast driving faces are main dust-producing sites in underground coal mines. The adoption of effective dust prevention and control measures is particularly important to suppress the production and diffusion of dusts in blasting driving faces.

In order to effectively suppress dust production and diffusion in blasting driving face, international scholars proposed different dedusting methods, mainly including dust removal by ventilation, spraying for dust removal, chemical suppression of dust, air curtain for dust isolation, and water-stemming for dust reduction (Ji et al. 2016; Fan et al. 2018). Unfortunately, due to the danger in blasting, insufficient knowledge of dust migration and distribution rules, and inaccurate technical parameters for dust removal, the dust

Responsible editor: Marcus Schulz

✉ Weimin Cheng
wmcheng@sdust.edu.cn

¹ College of Mining and Safety Engineering, Shandong University of Science and Technology, Qingdao 266590, China

² State Key Laboratory of Mining Disaster Prevention and Control Co-founded by Shandong Province and the Ministry of Science and Technology, Shandong University of Science and Technology, Qingdao 266590, China

suppression performances using the above methods are far from being ideal (Zhou et al. 2016a). Therefore, this paper thoroughly analyzed the diffusion and distribution rules of high-concentration dusts in the driving face after blasting, which helps to provide valuable theoretical references for dust prevention and control in the blasting driving faces.

Three methods have been mainly adopted for examining dust diffusion behaviors, namely, field measurement, numerical simulation, and experimental determination (Nie et al. 2016a). Among them, numerical simulation method is widely applied with increasing popularity because of several advantages it offers, including wide application range, strong operability, and low cost. Over the past years, researchers have performed extensive studies on the issue of coal dust in terms of both theory and application. Nakayama et al. (1996) simulated the migration of wind flow in the fully mechanized excavation face, and the numerical results of wind velocity were close to the measured data. However, the maximum wind velocity on the cross section was larger than the measured results. By combining field tests and numerical simulations, Toraño et al. (2011) investigated the migration rules of wind flow and the air-borne dust flow field under the forced-exhaust conditions on a 14.7-m² cross section in the fully mechanized excavation face. Using Monte Carlo method, Hu et al. (2015, 2016) constructed a gas-solid two-phase flow model to describe the particle motion and analyzed the spatial distribution of respirable dusts in a driving face after the blasting. However, due to the limitations in the solution model, the diffusion characteristics of the respirable dusts were incomprehensively investigated. Kurnia et al. (2014) utilize the computational fluid dynamic (CFD) approach to study dust dispersion and management in a driving face. Sa et al. (2012) established a model of dust migration based on the theory of gas-solid two-phase flow and the characteristics of the cavern stope. The dust concentration of the cavern stope changes due to ventilation every 20 min after blasting and the dust trajectory in different wind speeds were simulated by Fluent software. In the previous studies, the dust diffusion rules in a roadway were mainly investigated at a macro-scale. The limitations of dust number in simulations not only simplified the solution model but also made the solution dependent on empirical parameters. Thus, it is difficult to accurately analyze the diffusion characteristics of dusts in airflow field from a microscopic perspective.

The motion trajectory of dust particles in the airflow is intrinsically a gas-solid two-phase flow problem. Currently, two methods are mainly used in the numerical simulations on gas-solid two-phase flow. One is Euler-Euler method, also referred to as multiphase flow method, and the other is Euler-Lagrangian method, also referred to as particle trajectory method (Amritkar et al. 2014; Chen et al. 2015). Using Euler-Lagrangian method, the gas or liquid is treated as the background flow and the other phase is regarded as particles

distributed in this background flow. Then, the background is investigated using Euler method and the movement trajectory of the particle phase is tracked using Lagrangian method. Recently, a new coupling method combining discrete element model (DEM) and computational fluid dynamics (CFD), denoted as CFD-DEM, has been developed (Chen et al. 2015). Tsuji et al. (1992) for the first time proposed CFD-DEM method. They investigated the fluid flow via CFD and particle movement via DEM, and coupled the two methods to perform numerical simulations on the flow-solid two-phase flow. Compared with the traditional two-fluid model (TFM), CFD-DEM method is more suitable to gas-particle simulations (Han et al. 2015). Using this model, few empirical parameters are required, and the distribution of particle size can be conveniently considered. Moreover, the particle motion can be tracked in real time and the information can be accurately extracted. Some basic diffusion characteristics, including the drag force from the airflow, the dusts' spatial and temporal distributions, motion trajectory, and along-the-way settling characteristics, can be adequately analyzed at a micro-scale.

This study focused on a driving face in a footway in the south wing of Dongtan Coal Mine, Jining, China. According to the measured data, the mass concentration of the dusts in head-on region after the blasting was as high as over 1400 mg/m³ without any dust prevention measures. These high-concentration dusts can be spread more than 300 m away from the head-on region, which would severely threaten the coal miners' physical and psychological health. Based on the actual working conditions of this driving face, in the present study, an airflow-dust coupled model was established using CFD-DEM to further explore the dust diffusion and pollution mechanisms under two main ventilation conditions (namely, single-forced ventilation and single-exhaust ventilation).

CFD-DEM modeling of airflow and dust flow behavior

Airflow migration model

The airflow field formed in the blasting driving face was considered as a three-dimensional highly complex, unstable, and irregular flow with vortexes in a confined space (Nie et al. 2012). The air in the working face was regarded as incompressible and viscous, and the following continuity equation, momentum equation, energy equation, and gas state equation were adopted to describe this problem (Habeeb 2013):

$$\frac{\partial}{\partial x_i}(\rho u_i) = 0 \tag{1}$$

$$\frac{\partial}{\partial x_j}(\rho u_i u_j) = -\frac{\partial p}{\partial x_i} + \frac{\partial}{\partial x_j} \left(\mu \frac{\partial u_i}{\partial x_j} - \overline{\rho u'_i u'_j} \right) \tag{2}$$

$$\rho \frac{dh}{dt} - \frac{dp}{dt} = \frac{\partial}{\partial x_j} \left(\lambda \frac{\partial T}{\partial x_j} \right) - \frac{\partial}{\partial x_j} \left(\sum_s \rho_s h_s v_{sj} \right) + \frac{\partial q_{rj}}{\partial x_j} + \sum_s \rho_s g_j v_{sj} \tag{3}$$

$$p = \rho RT \tag{4}$$

where ρ denotes the gas density, with a unit of kg/m^3 ; x_i and x_j denote the coordinates along different directions in a Cartesian coordinate system, with a unit of m; t denotes time, with a unit of s; u_i and u_j denote the velocities along different directions in a Cartesian coordinate system, with a unit of m/s; p denotes the effective pressure, with a unit of Pa; μ denotes the dynamical viscosity coefficient, with a unit of Pa s; T denotes the temperature of airflow (or the smoke plume), with a unit of K; h denotes the airflow’s enthalpy, with a unit of J; v_{sj} denotes the airflow velocity, with a unit of m/s; q_r denotes the radiant heat of the smoke plume, with a unit of W; g_i and g_j denote the gravitational acceleration along the directions of i and j , respectively, with a unit of m/s^2 ; and R denotes the universal gas constant and has a value of 8.314 J/(mol K) .

The turbulence in the airflow in a blasting driving face is complex and nonlinear. In order to describe the flow with high strain rates or passing through the region with large curvatures, the RNG $k - \varepsilon$ turbulence model was constructed based on Reynolds averaging method. The k equation and ε equation can be written as (Habeeb 2013)

$$\frac{\partial}{\partial t} (\rho k) + \frac{\partial}{\partial x_i} (\rho k u_i) = \frac{\partial}{\partial x_j} \left(\sigma_k \mu_{eff} \frac{\partial k}{\partial x_j} \right) + G_k - \rho \varepsilon + S_k \tag{5}$$

$$\frac{\partial}{\partial t} (\rho \varepsilon) + \frac{\partial}{\partial x_i} (\rho \varepsilon u_i) = \frac{\partial}{\partial x_j} \left(\sigma_\varepsilon \mu_{eff} \frac{\partial \varepsilon}{\partial x_j} \right) + C_{1\varepsilon} G_k \frac{\varepsilon}{k} - C_{2\varepsilon} \rho \frac{\varepsilon^2}{k} \tag{6}$$

$$C_{2\varepsilon} \equiv C_{2\varepsilon} + \frac{C_{\mu} \rho \eta^3 (1 - \eta / \eta_0)}{1 + \beta \eta^3}$$

$$\mu_t = \mu_{t0} f \left(\sigma_s, \Omega, \frac{k}{\varepsilon} \right) \quad \mu_{t0} = \rho C_u \frac{k^2}{\varepsilon}$$

where $C_u = 0.0845$, $C_{1\varepsilon} = 1.42$, $C_{2\varepsilon} = 1.68$, $\sigma_s = 0.05$, $\sigma_k = \sigma_\varepsilon \approx 1.393$, $\eta = S_k/\varepsilon$, $\eta_0 = 4.38$, and $\beta = 0.012$; μ_{t0} and μ_t denote the turbulent viscosity coefficient before and after vortex modification, with a unit of Pa s; μ_{eff} denotes the diffusion coefficient; and Ω denotes the default estimated after the vortex was taken into account.

Modeling of dust flow

Since DEM was proposed, it has undergone rapid development in research field. However, its industrial applications were limited by computation capability and model accuracy. With the development of high-performance computation technology and modeling capacity, DEM has been gradually accepted by the industrial community (Akbarzadeh and Hrymak 2016). Using DEM, the external forces on the particles, such as gravity, virtual mass force, Magnus force, Brownian motion

force, the applied force in the flow field, and electromagnetic force, are added to the preset particle contact model framework, so that the motion acceleration and displacement of the particle in unit time step can be calculated (Akhshik et al. 2015). The transitional motion of a particle depends on the sum of forces acting on it, while the rotational motion is controlled by contact torques. Besides the liquid-solid interactions, drag force F_D , Saffman force F_{Saff} , and Magnus force F_M , the forces acting on particle, stem from particle-particle, particle-wall, and particle-impeller collisions (Hertz 1880), which are illustrated in Fig. 1.

$$m_i \frac{dv_i}{dt} = m_i g + \sum_{j=1}^{n_i} (F_{n,ij} + F_{t,ij}) + F_{D,i} + F_{M,i} + F_{Saff,i} \tag{7}$$

$$I_i \frac{d\omega_i}{dt} = \sum_{j=1}^{n_i} (T_{t,ij} + T_{r,ij}) \tag{8}$$

where v_i denotes the transitional velocity of particle, m_i denotes the mass of particle, $F_{n,ij}$ denotes the normal force, $F_{t,ij}$ denotes the tangential force, ω_i denotes the angular velocity of particle i , $T_{t,ij}$ denotes the torque between particles i and j generated by tangential forces, and $T_{r,ij}$ denotes the torque between particles i and j generated by radial forces.

The motions of the particles are independent of each other, and the interaction can only be generated when the particles contact each other. EDEM software provides a precise model, namely, HertzMindlin (nonslip) model that describes the contact force between particles, the contact force between particle and wall as well as the torque. The normal force $F_{n,ij}$ between particles i and j is (Shao et al. 2013)

$$F_{n,ij} = \frac{4}{3} Y^* \sqrt{R^*} \delta_{n,ij}^{3/2} - F_{n,ij}^d \tag{9}$$

$$F_{n,ij}^d = -\sqrt{\frac{5}{6}} \frac{\ln e}{\sqrt{\ln^2 e + \pi^2}} \sqrt{S_{n,ij} m^* v_n} \tag{10}$$

$$S_{n,ij} = 2Y^* \sqrt{R^*} \delta_{n,ij} \tag{11}$$

where Y^* is the equivalent Young’s modulus, m^* is the particle mass, R^* is the equivalent radius, $\delta_{n,ij}$ is the normal overlap,

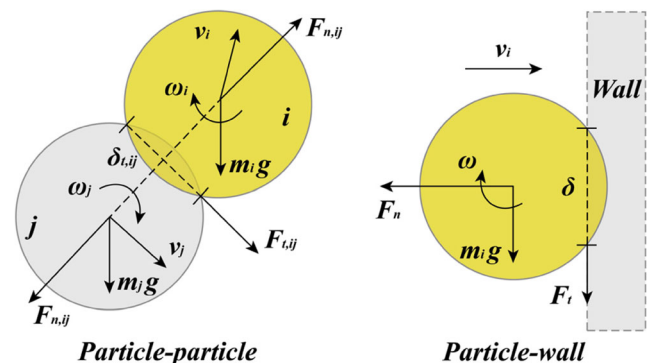


Fig. 1 Forces acting on particles during collisions

$S_{n,ij}$ is the normal stiffness, v_n is the normal component of the relative velocity, and e is the coefficient of restitution.

The tangential force $F_{t,ij}$ depends on the tangential overlap $\delta_{t,ij}$ and the tangential stiffness $S_{t,ij}$, and limited by Coulomb friction $\mu_s F_{n,ij}$, where μ_s is the coefficient of static friction and G^* is the shear modulus.

$$F_{t,ij} = -\delta_{t,ij} S_{t,ij} - F_{t,ij}^d \tag{12}$$

$$F_{t,ij}^d = -2\sqrt{\frac{5}{6}} \frac{\ln e}{\sqrt{\ln^2 e + \pi^2}} \sqrt{S_{t,ij} m^* v_t} \tag{13}$$

$$S_{t,ij} = 8G^* \sqrt{R^* \delta_{n,ij}} \tag{14}$$

The torques generated by the forces can be written as

$$T_{t,ij} = L_{ij} n_{ij} \times F_{t,ij} \tag{15}$$

$$T_{r,ij} = -\mu_r L_{ij} |F_{n,ij}| \frac{\omega_{ij}}{|\omega_{ij}|} \tag{16}$$

where L_{ij} is the distance from the center of particle i to the contact plane with particle j , n_{ij} represents the normal unit vector between two contacted particles, and ω_{ij} is the angular velocity vector of the object at the contact point.

Interaction between flow and dust

There exist extremely complicated interactions between the blasting-produced dusts and airflow. The forces on dusts exerted by the airflow mainly include drag force, buoyancy force, Saffman force, and virtual mass force. Since some forces are very small in the order of magnitudes compared with the others, they can be ignored (Ren et al. 2014). Then, only drag force, Magnus force, and Saffman force were considered. Meanwhile, the volume of dust particles is lower than 10% of the volume of the computational domain (Amritkar et al. 2014; Chen et al. 2011). Therefore, the counterforce of dusts on the airflow was negligible and only the force of stable airflow on dusts was taken into account. In this study, using API interface in EDEM software, the force characteristics of dust particles in the flow field were loaded into the solution framework of EDEM particle motion. The whole program was compiled in C++ language. The specific calculation method is described in detail below (Shao et al. 2013).

Saffman force denotes the force to lift the particle and it is induced by the flow velocities on both sides of the dust particle, and can be written as

$$F_{Saff} = 6.46B \sqrt{\rho_1 \eta R_d^2} \frac{(v_2 - v_1)(\nabla v_1)}{\sqrt{|\nabla v_1|}} \tag{17}$$

where B denotes an experimental constant, ρ_1 denotes the density of gas phase, η denotes the viscosity of gas phase, R_d denotes the radius of the particle, v_1 denotes the velocity

of gas phase, v_2 denotes the velocity of solid phase, and ∇ denotes the Hamiltonian operator.

The Magnus effect is induced when a spinning object moves in a fluid, and the Magnus force perpendicular to the line of motion is created by a whirlpool of fluid around itself. The Magnus force F_M is calculated as

$$F_M = 0.125\pi d_p^3 \rho_l \frac{Re_1}{Re_2} C_L [(0.5\omega_l - \omega_p) \times (\mathbf{u} - \mathbf{v})] \tag{18}$$

$$C_L = 0.45 + \left(\frac{Re_1}{Re_2} - 0.45\right) \exp(-0.05684 Re_1^{0.3} Re_2^{0.4}) \tag{19}$$

where $Re_1 = \frac{|\mathbf{u} - \mathbf{v}|}{\mu_l} d_p$, $Re_2 = \frac{|0.5\omega_l - \omega_p|}{\mu_l} d_p^2$, \mathbf{u} denotes the velocity vector, \mathbf{v} denotes the kinematic viscosity, ω_l is the local vorticity of liquid, and ω_p is the angular velocity of particle.

The drag force refers to the resistance of wind flow to the dust particle in gas-solid two-phase flow, and can be written as

$$F_R = (\rho_1 A_p C_d / 2) |v_1 - v_2| (v_1 - v_2) \tag{20}$$

where A_p denotes the projection of the particle in the direction perpendicular to the gas flow direction and C_d denotes the coefficient of viscous resistance.

Physical model and boundary conditions

The section of the footway in the south wing of Dongtan Coal Mine, Jining, China, is a three-element arch section, with a net width of 4.6 m, a net height of 3.54 m, and a net sectional area of 17.5 m². During the excavation process, the relative and absolute gas emission quantities are 0.09 and 1.22 m³/t, respectively, which categorizes the mine as low gas emission coal mine. The blasting dusts were mainly produced in the blasting process (the dusts produced in the preparatory phase before blasting and the subsequent loading and transportation process after blasting were not taken into account in this study), coals were crushed under the action of explosion work, and then, a great number of dusts were produced. The initial stage when the dusts entered the air was unstable. Since the solid dust particles greatly exceeded the air in inertia, the dust particles showed certain accelerations at the beginning of diffusion. Additionally, the dust production in blasting process was subjected to many factors such as blasting technology, explosive type, and charge. Therefore, the following two assumptions were made in this study: (1) the source dusts were uniformly distributed in the space 1.5 m away from the head-on section and (2) the dusts migrated along the positive direction of y axis at an initial velocity of 6 m/s (Chen et al. 2011).

Under normal conditions, two ventilation patterns, single-forced ventilation and single-exhaust ventilation, were used for dust discharge in a blasting driving face. When single-forced ventilation was used, the central axis of the forced air cylinder, with a diameter of 0.8 m, was 2.6 m away from the

floor, while the distance between the forced air outlet and the head-on section was 12 m. When single-exhaust ventilation was used, the central axis of the exhaust air cylinder, with a diameter of 0.7 m, was 2.5 m away from the floor, while the distance between the exhaust air outlet and the head-on section was 4 m. Additionally, the end of the exhaust air cylinder was connected with a dust removal fan, which was 40 m away from the head-on section. Both the forced air cylinder and the exhaust air cylinder were 0.1 m from the wall. The other devices such as cables, wires, water hoses, and forced air hoses were not taken into account in the model due to their small sizes. Figure 2 displays the constructed full-scale physical model. The positive direction of x axis denotes the direction from the central axis of the footway floor to the wall where the forced air cylinder was installed, the positive direction of y axis denotes the direction from the head-on section to the footway end, and the positive direction of z axis denotes the direction from the footway floor to roof.

According to the site actual ventilation conditions of the footway in the south wing of Dongtan Coal Mine, the basic boundary conditions of the airflow field were set as follows. Under both single-forced and single-exhaust ventilation conditions, the boundaries of the forced air inlet and the exhaust air inlet were set as “velocity inlet” (Nie et al. 2016a, 2016b). In order to guarantee the full development of the airflows on the end surface, the boundary of the footway’s end surface was set as “pressure outlet” at atmospheric pressure on site (Toraño et al. 2011; Hu et al. 2015). The walls of forced air cylinder, exhaust air cylinder, and the footway walls were all set as “no-slip.” Since the airflow velocity varies greatly near the footway wall, the semi-empirical standard wall function was used to correlate the physical quantities on the footway wall with the physical quantities in the core turbulence region. Moreover, the first grid node near the footway wall should be set in the layer of logarithm law. The forced air capacity and exhaust air capacity were set as 420 and 350 m³/min, respectively. In addition, the simulation was performed using ANSYS-Fluent under the following assumptions (Chen et al. 2013): (1) the temperature field is constant, (2) the fluid (air) is

incompressible, (3) the flow in the domain is fully turbulent, and (4) the footway and air cylinders were fixed. The solution model of airflow field and the related parameter settings are shown in the gray region in Table 1.

The dusts produced during the blasting in the driving face were irregular in shape and had a wide range in size distribution. Generally, the effects of particle shape on its motion characteristics are neglected in numerical simulations. The Rosin-Rammeler distribution function is used for characterizing the size distribution of dust particles. The measured results indicate that the dusts produced in the blasting ranged from 0.85 to 84.3 μm in diameter, with a median diameter and a distribution index of 12.1 μm and 1.93, respectively (Nie et al. 2016b; Erol et al. 2013). More than 10⁹ dust particles are produced in the blasting, and such huge number is well beyond the computation capacity of the DEM method (Feng and Owen 2014). In this study, 5000 dust particles were used to represent and characterize the overall migration behaviors of dusts after blasting. Furthermore, in order to gain in-depth knowledge of the motion characteristics of the dusts with different sizes in the footway, the dusts with some characteristic diameters were selected for further analyzing the motions of particles, which would be of great value to elaborate the overall motion characteristics of dusts after blasting. Since PM_{2.5} is an important index in measuring and controlling air pollution degree and the dusts with a diameter smaller than 7 μm primarily accounted for pneumoconiosis (Zhou et al. 2017), additionally, the measured results indicate that the characteristic particle diameter (the diameter of the dust particles occupying 62.5% of total dust particles in mass) was approximately 20 μm, and the dust particles have a diameter range of 0.85–84.3 μm; i.e., 40 and 80 μm were approximately half and total value of the whole diameter range (Nie et al. 2012). Accordingly, this study selected five types of dusts for analysis, with the characteristic diameters of 2.5, 7, 20, 40, and 80 μm. According to the physical properties of coals in the footway and the field working conditions, the simulation parameters in DEM were set, as shown in the blue region in Table 1.

Fig. 2 Illustration of the constructed physical model

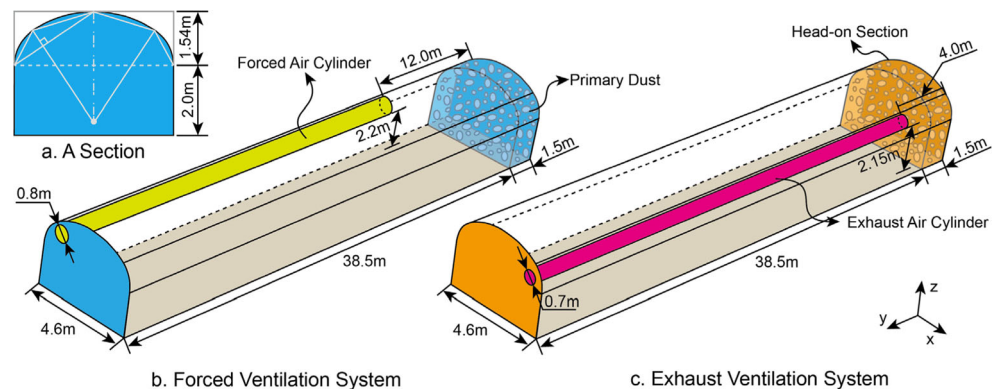


Table 1 Parameter settings in the present simulation using CFD-DEM

Type	Property	Value/property	Type	Property	Value/property
General	Solver type	Pressure-based	Viscous model	k-epsilon (RNG)	Realizable
	Time	Transient		Near-wall treatment	Standard wall function
Air	Density	1.225 kg/m ³	Pressure outlet	Pressure outlet	1.1 atm
	Viscosity	1.79E-05 Pa-s		Tunnel and equipments	Wall
Solution methods	Scheme	SIMPLE	Calculation	Time step size	0.0001s
	High-order term relaxation	ON		Max iteration step	40
Forced air outlet	Velocity inlet	13.93 m/s	Exhaust air inlet	Velocity inlet	-15.17 m/s
	Turbulent intensity	2.93%		Turbulent intensity	2.96%
	Hydraulic diameter	0.8 m		Hydraulic diameter	0.7 m
Solver model	Particle-particle	HerzMindin (no slip)	Particle material	Particle density	1400 kg/m ³
	Particle-geometry	HerzMindin (no slip)		Poisson's ratio	0.5
	Body force	API coupled interface		Shear modulus	1E8 Pa
Particle	Radius	Rosin-Rammler		Recovery coefficient	0.5
Simulation	Fixed time step	1.00E-07 s		Static friction coefficient	0.4
	Cell size	48 mm		Rolling friction coefficient	0.05

Mesh independence study

The generation of finite element meshes is an essential step in numerical simulations since it directly affects the accuracy of the subsequent numerical calculation (Wang and Ren 2013). Mesh generation includes the selection of unit type and the determination of grid density. Hexahedral mesh is suitable for the present physical model, and is selected owing to high efficiency and mesh quality (Jiang et al. 2013). Thus, based on ICEM CFD mesh generation tool, the discrete mesh model was established using “top-down” block topology construction method; meanwhile, the closeness degree of the mesh was adjusted in trial computations. More meshes would lead to smaller discrete errors but also may reduce the solution speed and increase the round-off errors. Therefore, it is beneficial to conduct the mesh independent study so as to ensure that both the discretization and round-off errors are

within acceptable level and the solution does not vary significantly with the mesh adopted (Wang and Ren 2013).

In this study, the hexahedral discrete meshes with three different densities, which represent excellent, good, and moderate meshes, were generated using ICEM CFD. The mesh quality was greater than 0.5 for all the mesh densities. Since the airflow fields in different positions show great differences, four footway sections that can reflect the airflow field characteristics were selected along the direction of *y* axis, which were 5, 10, 20, and 30 m away from the head-on section. Additionally, the airflow velocities at *z*=2.0 m were compared for the three densities in order to examine the effects of mesh density on computation results, as shown in Fig. 3. It can be found that the airflow velocities in these three meshes showed similar variation trend. The simulation results from good mesh and excellent mesh were close to each other, and both differed greatly from the results from moderated mesh.

Fig. 3 Comparison of the simulation results using meshes of different densities

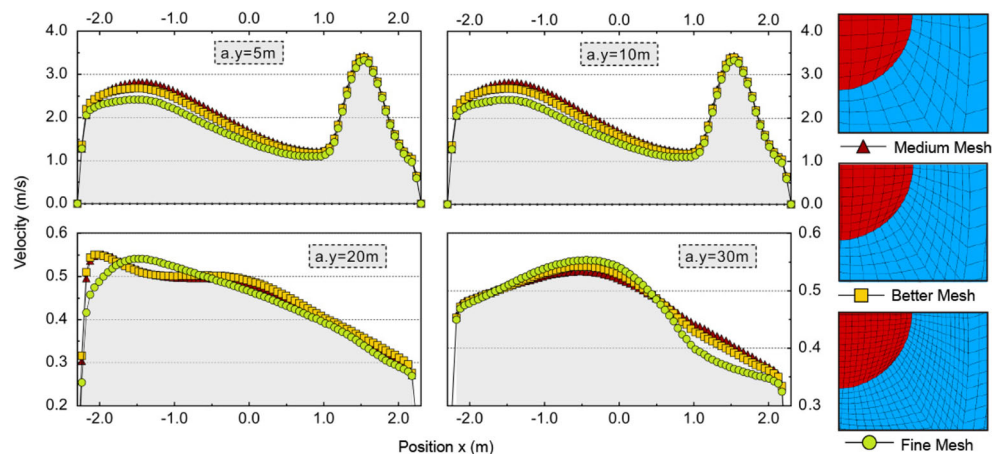
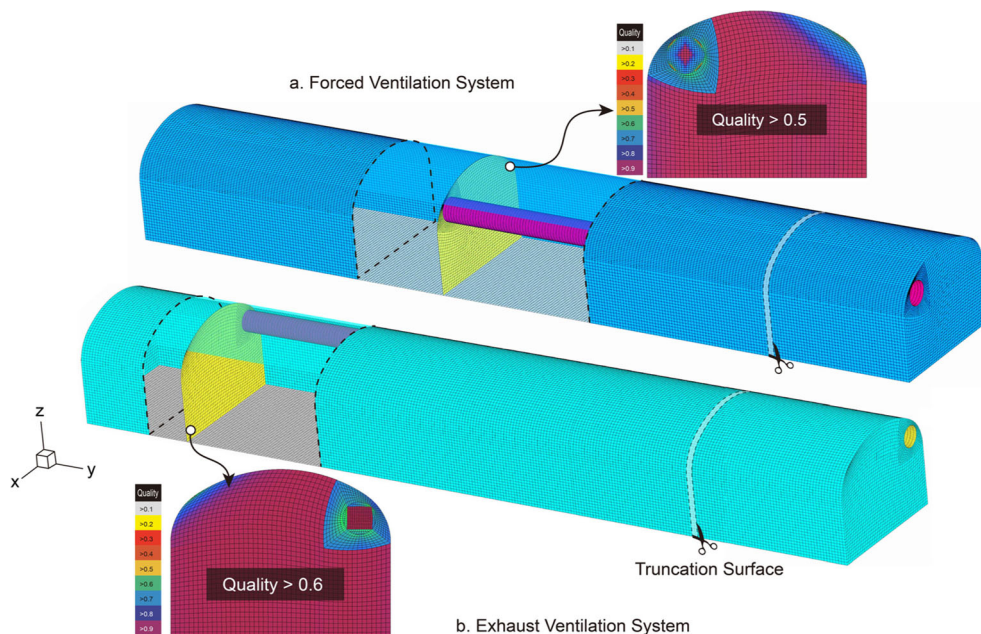


Fig. 4 Meshed geometries



Thus, it can be concluded that good mesh can satisfy the independence requirement of the mesh and ensure the accuracy of airflow field and dust field simulations. Figure 4 shows the mesh generation results.

Validation of base model

Both modeling error and numerical error can affect the accuracy of numerical simulation results (Wang et al. 2015a). In order to validate the accuracy of CFD-DEM coupling model, the airflow velocities and dust concentrations in the test footway under both single-forced and single-exhaust ventilation conditions were measured on site. According to the footway size and the actual blasting conditions, eight sections in total were selected for dust measurements, where were 5, 10, 15, 20, 25, 30, 35, and 40 m away from the head-on section; eight measurement points (denoted as $C_1 \sim C_8$) were uniformly arranged on each section, as shown in Fig. 5. In this study, the accuracy of the constructed model was validated through the comparison between the field measured results and the simulation results under single-forced ventilation conditions. As shown in Fig. 6, the airflow velocities at different measuring points under two different ventilation conditions were measured by the airflow velocity sensors (TSI8455). As to the measurement of dust concentration, the anti-explosion, direct-reading dust-measurement instruments for mines (CCZ-1000) were used, as shown in Fig. 7, and the dust concentration at each section was acquired by taking the average of the concentrations at eight measurement point (Nie et al. 2016a). By using the dust concentration 5 m away from the head-on section as the source dust concentration, the ratio of

the mass of the dusts that passed each section to the mass of the source dusts was calculated, denoted as the dust passing ratio at each section. The measured results of dust passing ratio were then compared with the results extracted by Analyst module, as shown in Fig. 8.

According to the field measured results, the airflow velocity was high at the head-on section, then decreased gradually along the direction of y axis, reached a peak approximately 15 m away from the head-on section, and finally stabilized at a low value. The simulation results using CFD matched the measured airflow velocities, suggesting that the concluded airflow migration rules in the blasting working face were basically accurate. However, the measured results deviated from the simulation results by 0.15~14.12%. A lot of uncontrollable

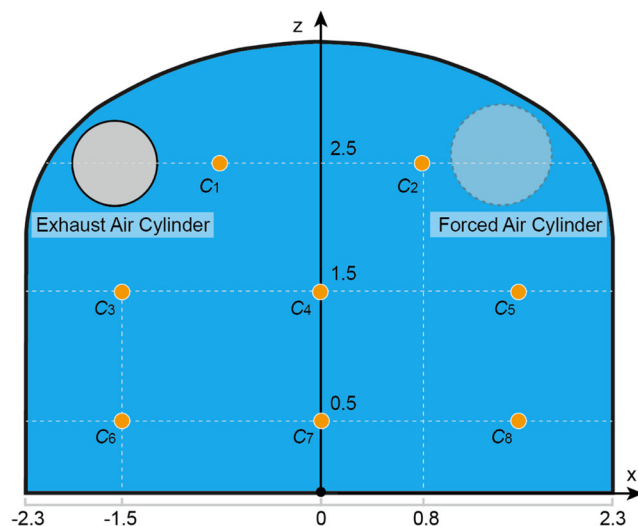


Fig. 5 Layout of the measurement points at each section

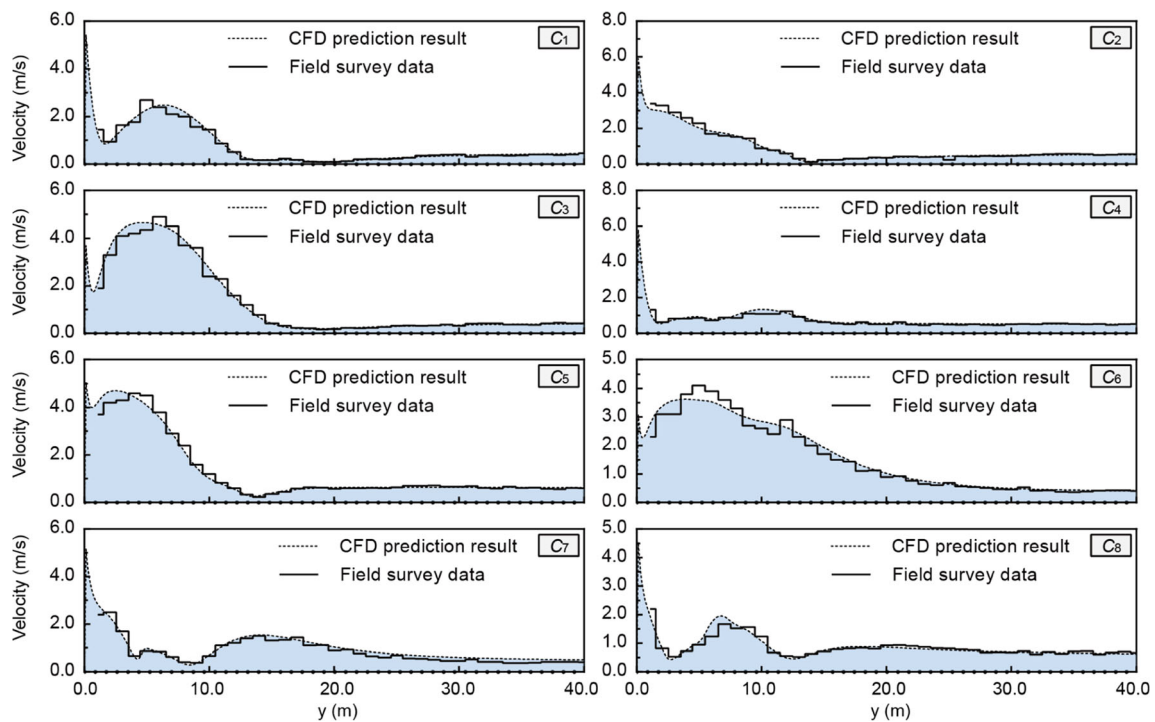


Fig. 6 Comparison between the measured results of airflow field and the simulation results

factors in the air supply instruments and environmental conditions in the working face contributed to the deviation. Generally, a relation deviation smaller than 15% is acceptable (Nie et al. 2016b; Wang et al. 2015b), which means that the present numerical simulation results of the airflow field are accurate.

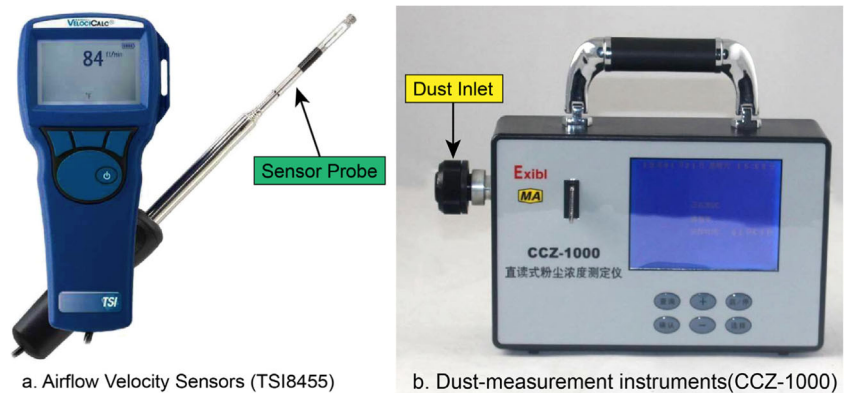
As shown in Fig. 8, both the measured values and the simulation results of the dust passing ratios at various sections decreased as the distance from the head-on section increased along *y* axis. The relative deviations between the measured dust passing ratios and the simulation results ranged from 0 to 17.82%. Especially, the deviations exceeded 15% at the sections 20 and 25 m away from the head-on section. Since many factors in the blasting can affect the dust production and the dust

measuring method show certain limitations, the relative deviations can thus be neglected (Nie et al. 2016a; Wang et al. 2015b). Therefore, the simulation results of airflow-dust coupling based on CFD-DEM were accurate.

Discussion and analysis

The dusts produced in blasting were carried by the airflow and thus spread to the other regions in the working face. In order to understand the dust diffusion and pollution mechanisms, the migration rules of the airflow field should be firstly analyzed. Based on the established airflow field model using FLUENT, this study then conducted the simulations on the migration of

Fig. 7 Airflow speed and dust concentration determination equipment



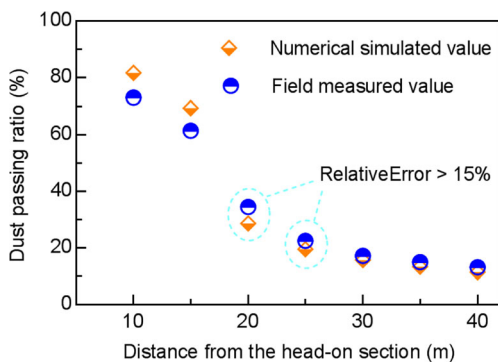


Fig. 8 Comparison between the measured dust concentrations and the simulation results

airflow field in the footway under two different ventilation conditions.

Analysis of the numerical simulation results of the migration of airflow field

As shown in Fig. 9, under single-forced ventilation condition, the high-velocity air was ejected from the forced air outlet, and then, a high-velocity jet flow field was formed. Momentum was transferred from high-velocity air and the surrounding air via shear force, leading to the expansion of jet flow section. While flowing towards the negative direction of *y* axis, the air hit the head-on section and was then bounced back towards the positive direction of *y* axis. Due to energy loss, the airflow velocity decreased somewhat but still remained above 3 m/s,

as shown in Fig. 9, where the iso-velocity contour of 3 m/s was marked. Strong negative pressure was generated around the forced outlet because of the large airflow velocity in this region. Then, a portion of the air moving backward had a velocity component along the positive direction of *x* axis, while another portion of the air moved into the jet flow field due to entrainment effect, thus forming a vortex airflow field in the region from the forced air outlet to the head-on section. Additionally, the rest of the air was gradually spread from the forced air cylinder to the whole footway section, and the airflow gradually stabilized. According to the above analysis, the airflow field under single-forced ventilation condition can be divided into three regions, namely, vortex region (0~12 m away from the head-on section), multi-direction turbulence region (12~17 m away from the head-on section), and stable region with a same direction (17~30 m away from the head-on section) (Wang 2011; Pandey et al. 2008). From Fig. 10, it can be observed that, under single-exhaust ventilation condition, a region of relatively high negative pressure was formed around the exhaust air inlet. Moreover, the negative pressure decreased in magnitude gradually and the air velocity gradually decreased as the distance away from the exhaust air inlet increased. In the region from the footway end to the exhaust air outlet, the airflow direction basically pointed to the negative direction of *y* axis. In the region from the exhaust air inlet to the head-on section, the airflow pointed solely towards the exhaust air inlet because of large negative pressure. Forty meters away from the head-on section, the airflow velocities basically maintained at approximately 0.4~0.5 m/s, with iso-

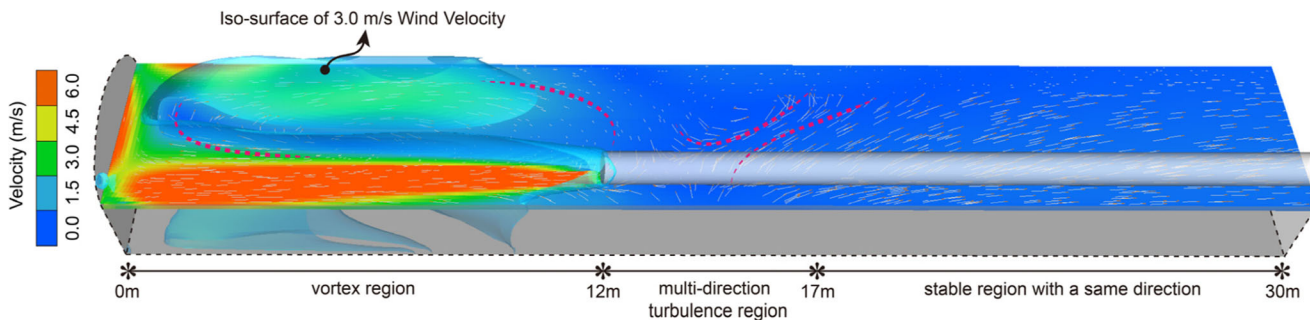


Fig. 9 Airflow field in the footway under single-forced ventilation condition

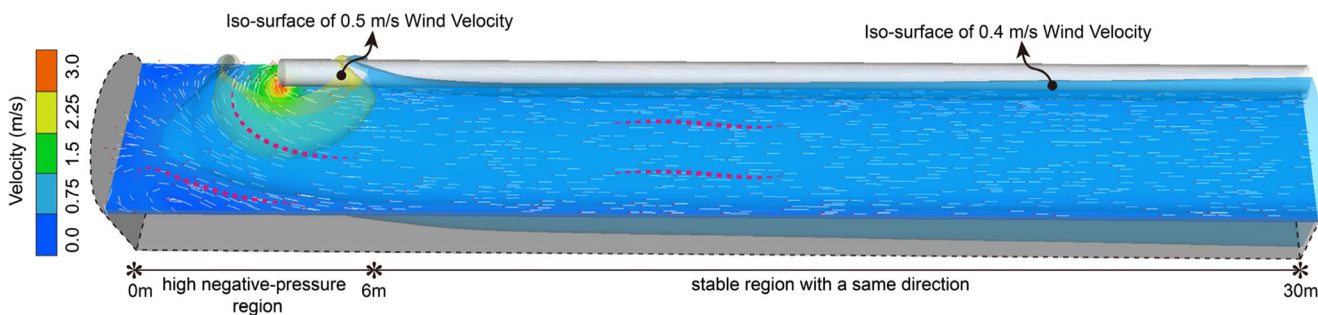
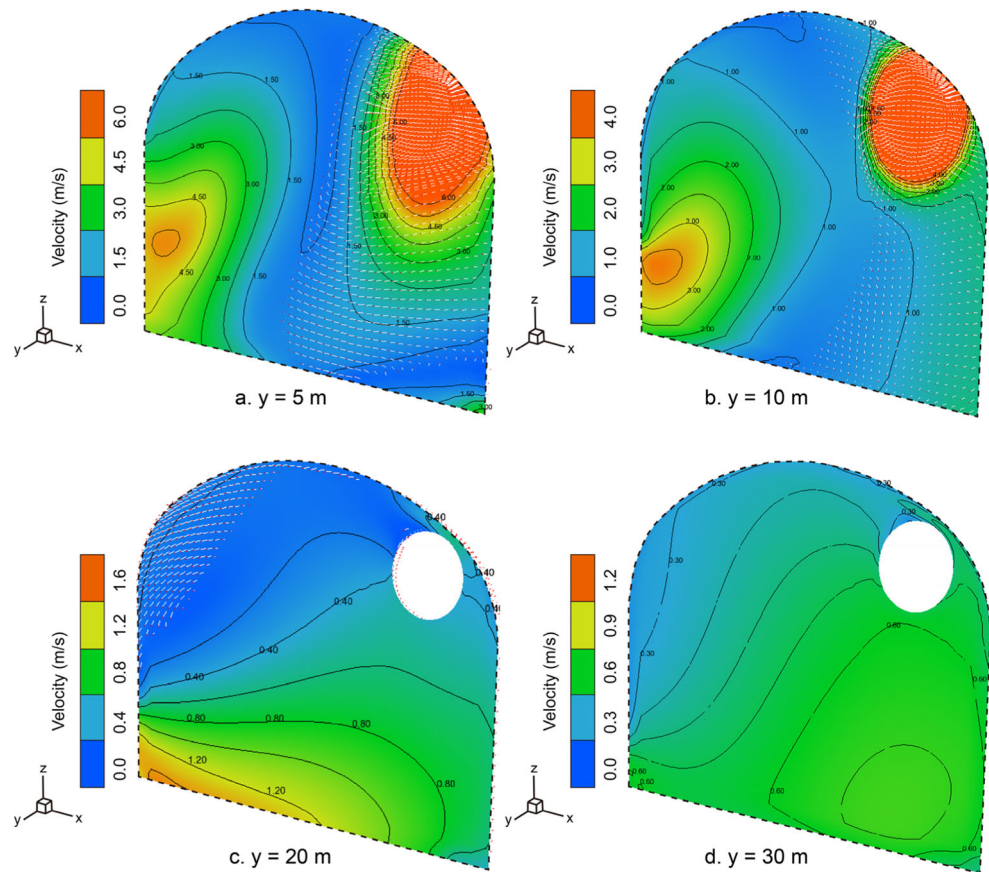


Fig. 10 Airflow field in the footway under single-exhaust ventilation condition

Fig. 11 Simulation results of airflow field under single-forced ventilation condition

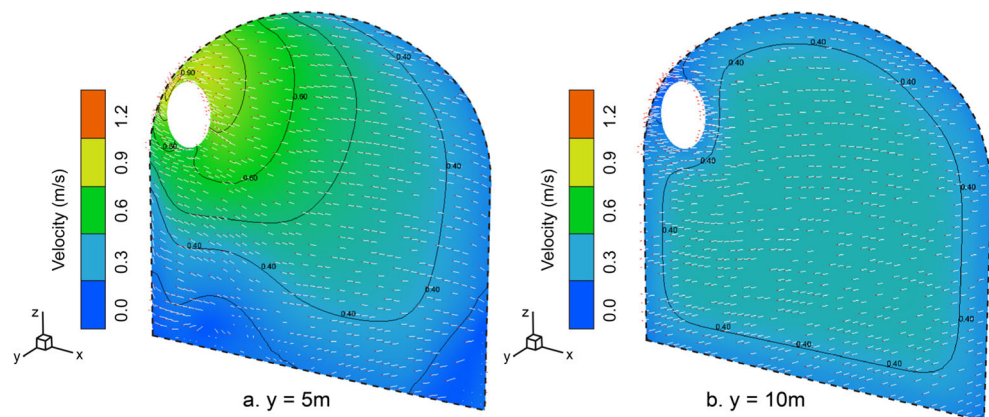


velocity contours of 0.4 and 0.5 m/s marked in Fig. 10. Accordingly, the airflow field under single-exhaust ventilation condition can be divided into a high negative-pressure region (0~6 m away from the head-on section) and a stable region with a same direction (6~30 m away from the head-on section) (Petrov et al. 2014).

After the blasting, the produced dusts mainly migrated towards the positive direction of *y* axis, and the airflow distributions and directions at different sections along *y* axis were then analyzed. According to the above-described airflow characteristics under different ventilation conditions, different

sections along the footway, as shown in Figs. 11 and 12, were selected for further analysis. It can be observed that (1) under single-forced ventilation condition, as the distance away from the head-on section increased, the airflow direction gradually changed from the positive direction of *y* axis to the negative. Ten meters away from the head-on section, the high-velocity airflows were mainly distributed in the forced jet flow field and the region of rebounded air. The air near the forced air cylinder flowed through approximately 30% of the footway. As the airflow migration distance increased, both the flow area along the negative direction of *y* axis and airflow velocity

Fig. 12 Simulation results of airflow field under single-exhaust ventilation condition



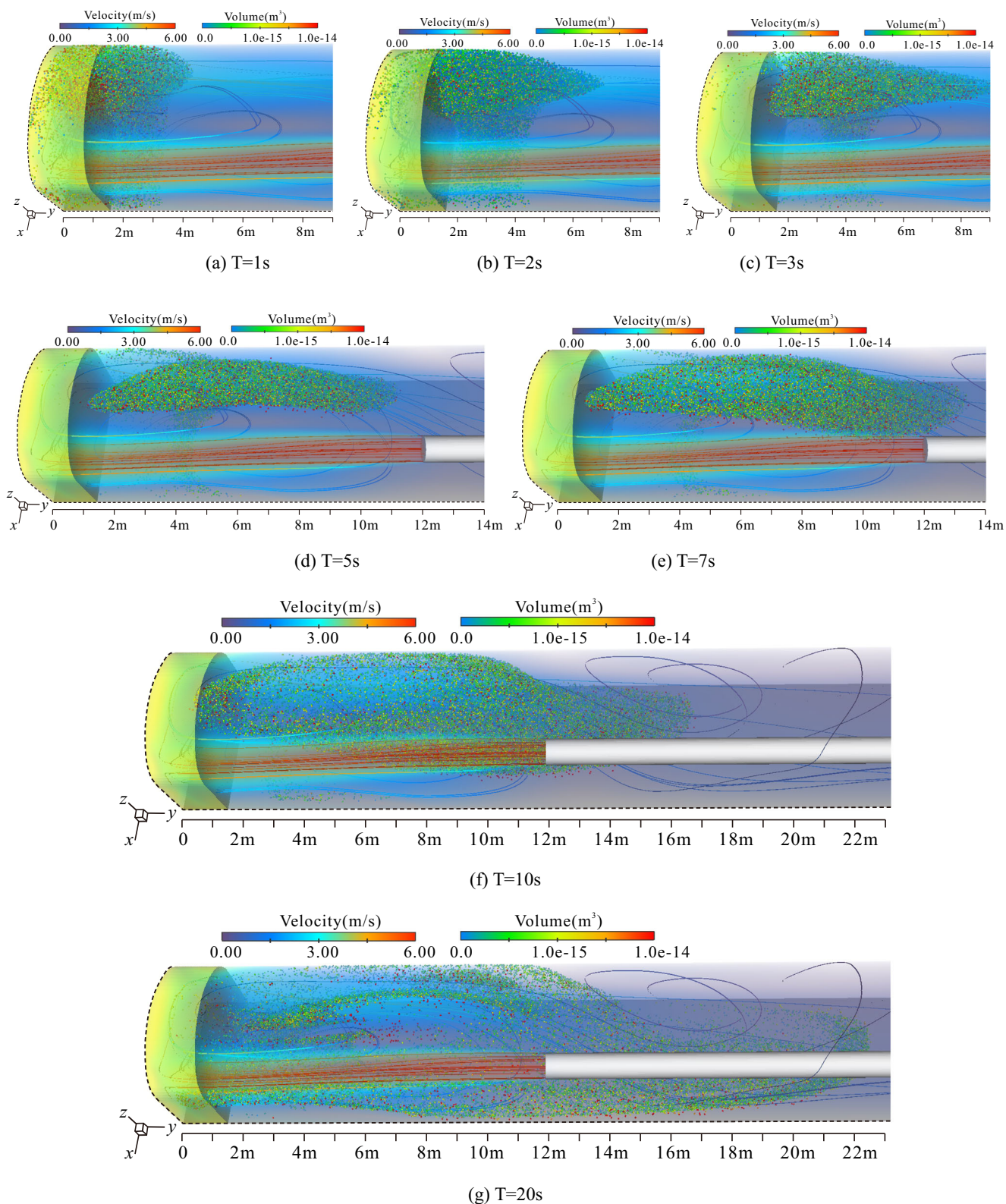


Fig. 13 Simulation results of the airflow-dust coupled migration at different time under single-forced ventilation condition, where **a** $T=1$ s, **b** $T=2$ s, **c** $T=3$ s, **d** $T=5$ s, **e** $T=7$ s, **f** $T=10$ s, **g** $T=20$ s, **h** $T=50$ s, **i** $T=100$ s, **j** $T=200$ s, and **k** $T=300$ s

decreased gradually, while the airflow velocity was relatively large near the footway floor. At the section of $y=20$ m, the

airflow around the floor moved along the negative direction of y axis, with a flow area of approximately 10% of the footway.

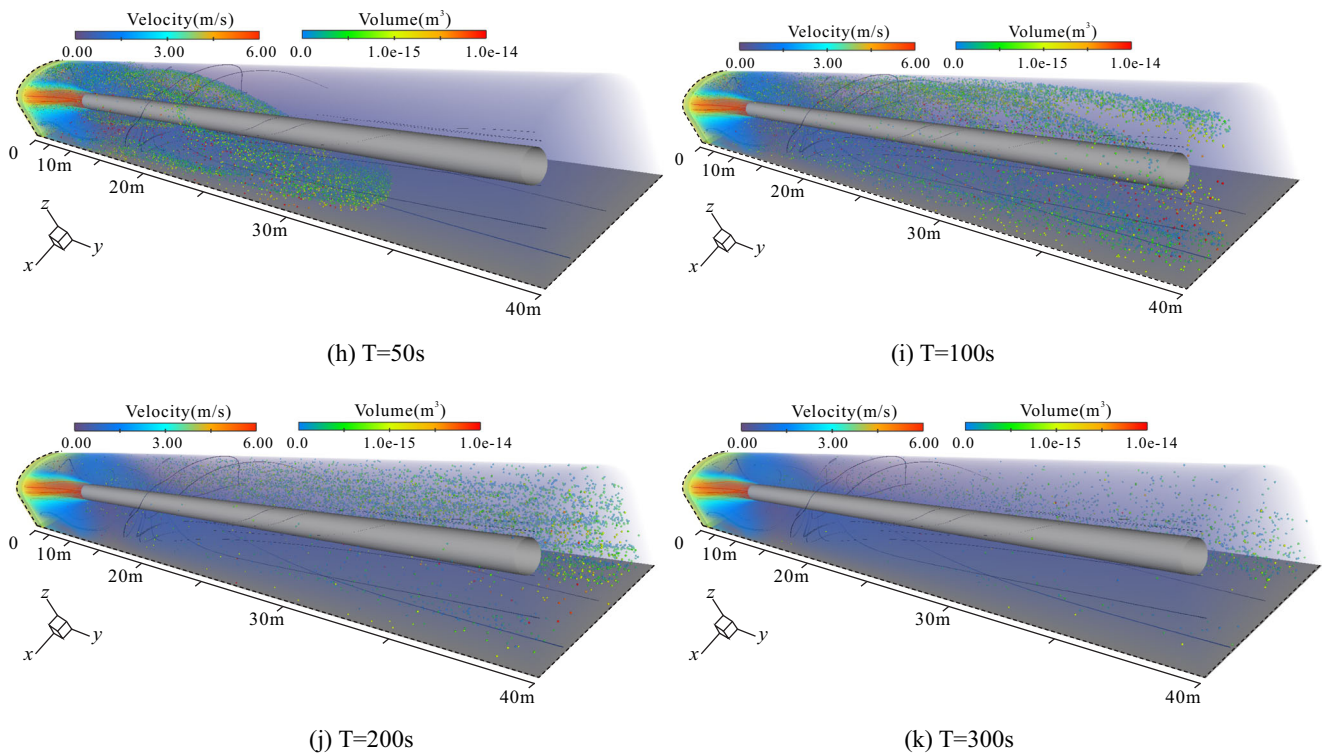


Fig. 13 continued.

At the section of $y = 30\text{ m}$, the airflow pointed to the positive direction of y axis, and the airflow velocities tended to be stable at around $0.3\text{--}0.6\text{ m/s}$. (2) Under single-exhaust ventilation condition, the airflows at the sections of $y = 5\text{ m}$ and $y = 10\text{ m}$ both pointed to the negative direction of y axis. The nearer the distance from the forced air outlet is, the greater the difference between airflow velocities at a section is. At the section over 10 m away from the head-on section, the airflow velocity reached a stable value of approximately 0.4 m/s .

Analysis of the numerical simulation results of the migration of airflow-dust coupled field

A great mass of dusts was produced in quite short time after the blasting. The high-concentration dusts rapidly filled the whole throwing belt, and then migrated along the axial direction of the footway under the action of airflow drag force (Qin et al. 2011). In order to gain in-depth knowledge of the dusts’ diffusion and migration rules, some representative moments were selected for analyzing the airflow-dust coupled migration under both single-forced and single-exhaust ventilation conditions, as shown in Figs. 13 and 14. Since the dust particles were quite small in size, they were amplified for better display of dust distribution. Moreover, the dusts with different volumes (unit m^3) were marked by different colors. To further show the effects of airflow on the migration of dust particles, 15 airflow lines were extracted for

characterizing the distribution of airflow field, as shown in Figs. 13 and 14, in which different airflow velocities, with a unit of m/s , were marked by different colors.

Effects of drag force in the airflow field

As shown in Fig. 13, under single-forced ventilation condition, the airflow drag force played an important role in the migration of dusts produced by blasting (Kim et al. 2006). At the first 5 s in the diffusion, the dust particles mainly gathered in the rebound air region. Due to the entrainment effect, some dusts began to migrate towards the negative direction of x axis at 7 s . This generated migration momentum towards the negative direction of x axis, and the other dusts were spread rearward with the high-velocity airflow at the footway floor. As the diffusion distance increased, the airflows gradually filled the whole footway section, and the dust particles also gradually diffused to the whole section, as shown in Fig. 13i. After 300 s of dust diffusion, more than 93% of the dusts moved out of the computational domain or settled. At the diffusion time of 620 s , the dust particles in the footway almost disappeared. As shown in Fig. 14, under single-exhaust ventilation condition, at the first 5 s in the diffusion, most of the dusts were far from the exhaust air inlet and subjected to the impact of weak negative pressure. By contrast, the dusts at the footway roof were near the exhaust air inlet, and most of them were then sucked into the exhaust inlet. As the diffusion distance along the

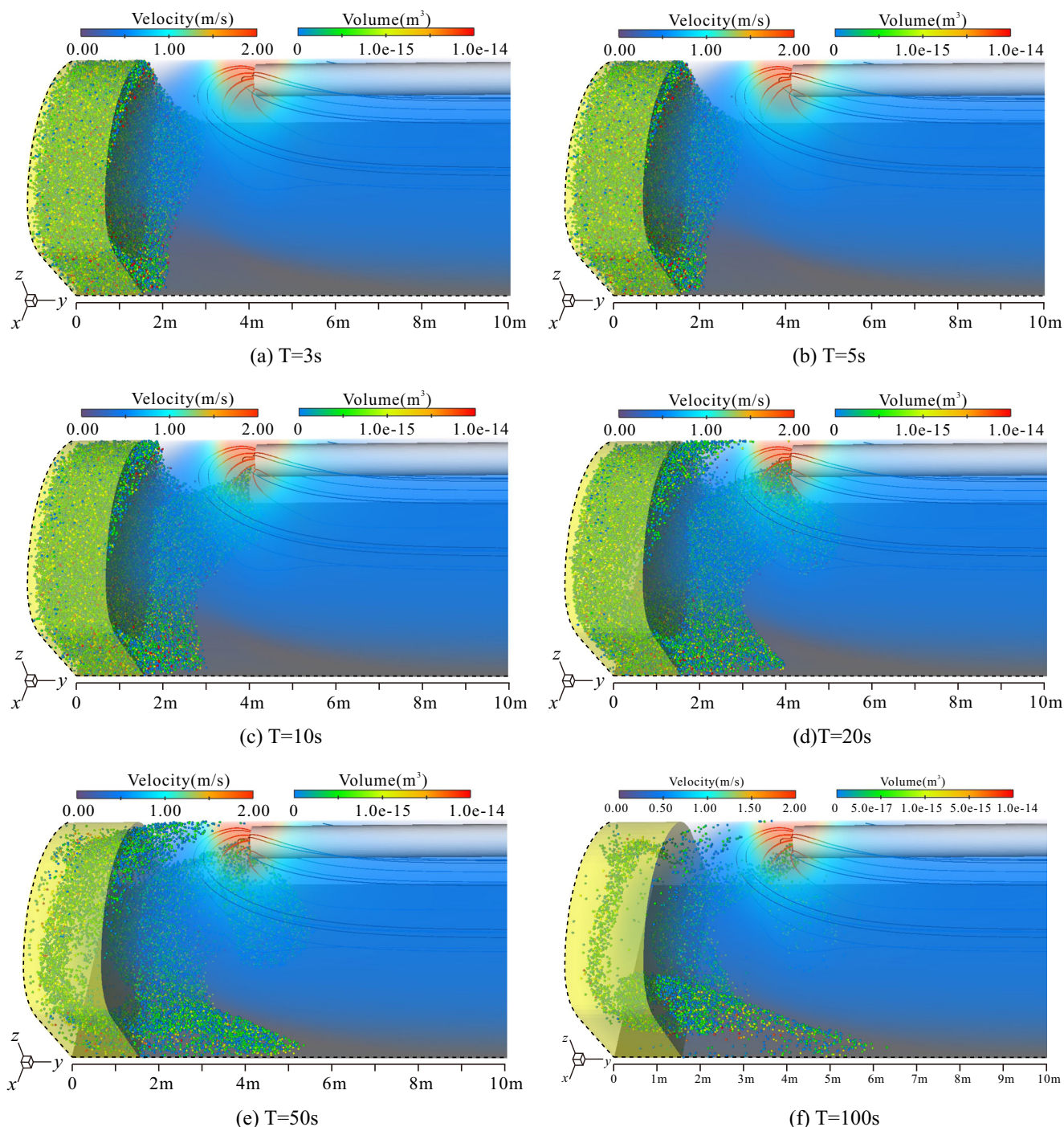


Fig. 14 Simulation results of the airflow-dust coupled migration at different time under single-exhaust ventilation condition, where **a** $T = 3$ s, **b** $T = 5$ s, **c** $T = 10$ s, **d** $T = 20$ s, **e** $T = 50$ s, and **f** $T = 100$ s

positive direction of y axis increased, the negative-pressure impact at the exhaust air inlet strengthened. Some dusts gradually moved up and were then sucked into the exhaust air cylinder. The dusts near the footway wall where the forced air cylinder was located were impacted by weak negative pressure and were completely settled at a location 6 m away from the head-on section. At the diffusion time of 720 s, no dusts were left in the footway.

The effect of ventilation conditions on the migration of dust particles can hardly be analyzed comprehensively merely using the simulation results of airflow-dust coupled migration. Thus, the motions of single dust particle with the diameter of 2.5, 7, 20, 40, and 80 μm under both single-forced and single-exhaust ventilation conditions were analyzed, which were then compared with the airflow streamline for exploring the effect of airflow field drag force on the migration of dusts with different

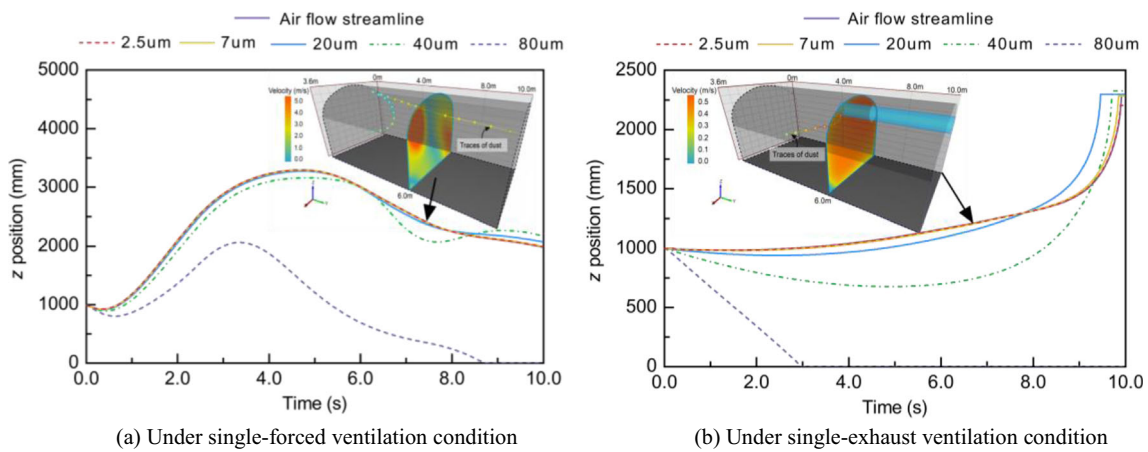


Fig. 15 Comparison between the motion trajectories of the dusts with different diameters and airflow streamline, **a** Under single-forced ventilation condition and **b** under single-exhaust ventilation condition

diameters. First, single dust particle was statistically generated at the coordinate point (0, 1000, 1000), and the variation of *z* component of the single dust particle within 10 s was acquired and shown in Fig. 15. Under single-forced ventilation condition, the motion trajectories of the dust particles with the diameter smaller than 40 μm closely followed the airflow streamline. Especially, the motion trajectory of 2.5 μm dust particle completely matched the airflow streamline, suggesting that the airflow field significantly affected the migration of these dust particles. However, the dust particles with a diameter over 80 μm were mainly subjected to gravity. The airflow drag force was outbalanced by gravity. Under single-exhaust ventilation condition, the motion trajectories of the dust particles smaller than 20 μm were close to the airflow streamline. In particular, the motion trajectory of 2.5-μm dust particle closely followed the airflow streamline. The motion trajectory of the dust particle with a diameter of 40 μm significantly deviated from the airflow streamline, and the motion trajectory of the dust particle with a diameter over 80 μm linearly decreased with the diffusion time, indicating that the airflow drag force was fairly weak and the dusts settled uniformly along *z* axis.

Motion trajectories of the dusts

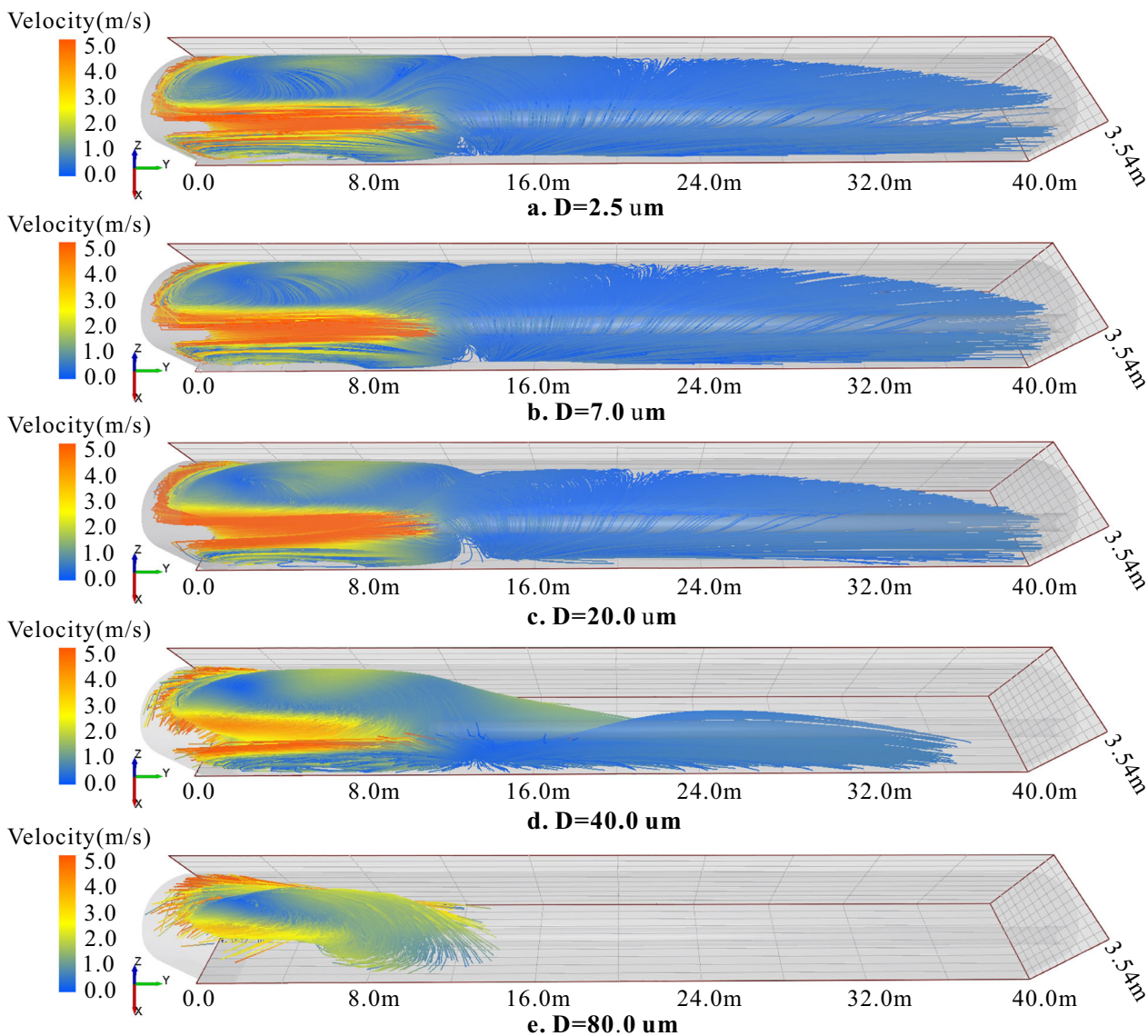
The dusts were not only subjected to the effects due to the external environment and the inherent collision force but also affected by the air medium and flow condition (Zhou et al. 2016b; Xie et al. 2007), thus showing relatively complex motion trajectories in the air. Under complex actions and effects, the dusts with different diameters had different motion trajectories. In order to analyze the motion trajectories of the dusts with different sizes under different ventilation conditions, the motion trajectories of the dusts with different diameters were acquired using the post-processing module in EDEM, as shown in Fig. 16. Under single-forced ventilation condition, the dusts with different diameters showed similar motion trajectories. Thirteen meters away from the head-on section, the

vortex effects came into play for dust particles with the diameter of 2.5~80 μm. Eighty-micrometer dust particles were significantly affected by gravity and thus only showed diffusion within the vortex flow field, while the dusts smaller than 40 μm migrated backward along the footway roof. Forty-micrometer dusts were close to the footway wall where the forced air cylinder was located and settled gradually at the location 16~36 m away from the head-on section. The dusts with a diameter smaller than 20 μm were still close to the footway. They gradually spread to the whole footway section and thus polluted the region at the end of the footway. Under single-exhaust ventilation condition, the dusts with different diameters also showed similar motion trajectories. In the region 0~3 m away from the head-on region, the dusts slowly migrated towards the positive direction of *y* axis, and large dusts had high migration velocities along *z* axis due to gravity effect. In the region 3~5 m away from the head-on section, some dusts with the diameter of 2.5~40 μm moved up rapidly and were eventually sucked into the exhaust air cylinder with the increase of velocity. For the dusts with a diameter over 80 μm, the motion trajectories followed a parabola pattern due to the influence of gravity, and settled within the range 3 m away from the head-on section.

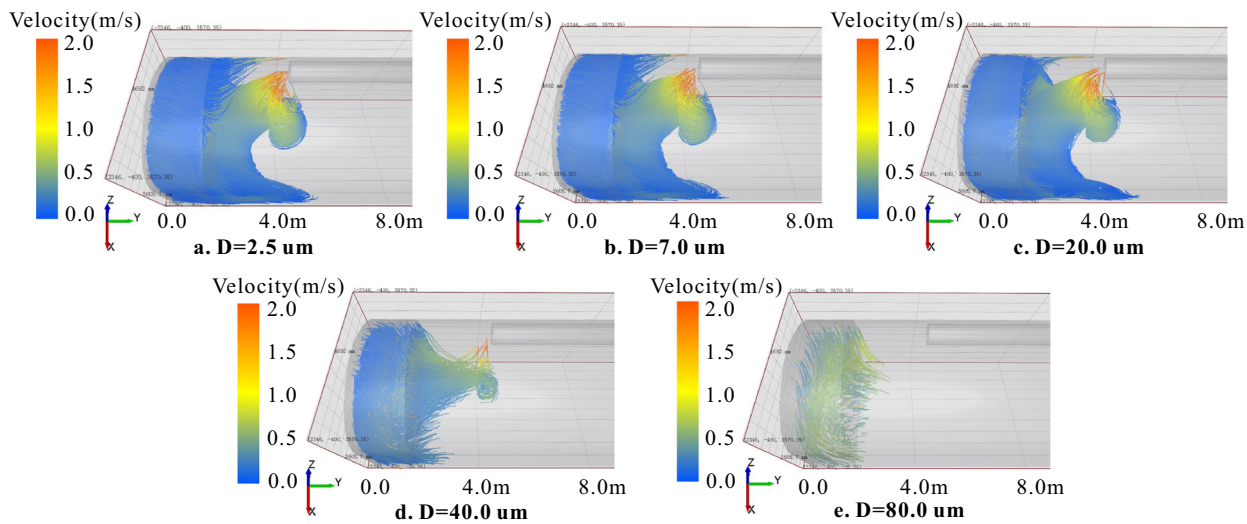
Negative-pressure-induced dust emission ratio

Under single-exhaust ventilation condition, the effects of exhaust-induced negative pressure on the dusts mainly depended on dust particle diameter and the distance from the exhaust air inlet (Zheng et al. 2009; Zhou et al. 2017). Using the function of “Grid Bin” in the “Analyst” module, the cumulative dust emissions were calculated, as shown in Fig. 17.

Fig. 16 Motion trajectories of the dusts with different diameters under different ventilation conditions, **a** under single-forced ventilation condition and **b** under single-exhaust ventilation condition



(a) Under single-forced ventilation condition



(b) Under single-exhaust ventilation condition

It can be observed that, with the increase of diffusion time, the dust emission velocity decreased gradually, and the dusts with diameters of 2.5 and 7 μm showed similar variation trend of dust emission ratios. After approximately 100 s of diffusion, the dust emission ratios tended to stabilize after 40 s of diffusion for 20-μm dusts and 20 s for 40-μm dusts. Thus, it can be concluded that the dusts with a larger diameter stabilized more quickly. Moreover, smaller dusts had larger cumulative amount of dust emission. The dust emission ratio was up to 76.86% for 2.5-μm dusts, and the dust emission ratio was up to 74.36% for 7-μm dusts. Almost no dusts were discharged for a diameter over 80 μm. Through nonlinear fitting, the dust particle diameter (D) and the negative-pressure-induced dust emission ratio (P) show the following relationship: $P = -25.03\ln(D) + 110.39$.

Spatial and temporal distributions of dust

After the blasting, the generated dusts showed complex diffusion motions in the air, and significantly different distributions at different times (Chen et al. 2013; Ren and Qin 2013). Thus, understanding the spatial and temporal distribution rules of the dusts in real time can provide effective theoretical references for dust prevention and control. In order to analyze the characteristics of the dust distribution in 3D space, the footway space was divided into different statistic units (each with a size of 0.5×0.5 m) in horizontal plane and vertical plane. The cumulative numbers of the dusts with different diameters in different units were calculated for analyzing the main accumulation regions.

(1) Distribution of dusts in horizontal plane

Figure 18 shows the numbers of the cumulative dust particles with different diameters in horizontal plane. It can be observed that, under single-forced ventilation condition, the dusts with different diameters showed different distribution in horizontal plane. Specifically, under both the vortex airflow

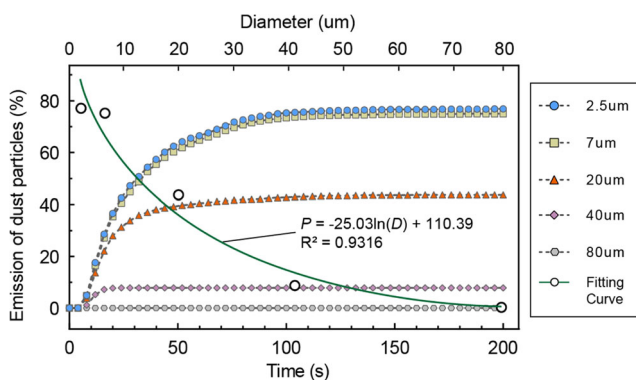


Fig. 17 Negative-pressure-induced emission ratios of the dusts with different diameters at different times and the fitted curves

field in front of the head-on section and the entrainment effect around the forced air outlet, a great number of the dusts with the diameter smaller than 20 μm accumulated in front of the head-on section (5 and 17–25 m away from the head-on section, respectively). Since gravity impact was significant, most of the dusts with the diameter of 40 μm concentrated in the region 5 m away from the head-on section, while the rest of dusts were spread to the region 35 m away from the head-on section along the footway wall near the forced air cylinder. The dusts with a diameter of 80 μm were also distributed in the region 13 m away from the head-on section. Under single-exhaust condition, the exhaust-induced negative pressure imposed a strong impact on the dusts near the footway wall where the exhaust air cylinder was located, but it slightly affected the dusts on the other side of the footway wall. Hence, the dusts with a diameter smaller than 20 μm were mainly distributed near the footway walls. Of the dusts with a diameter of 40 μm, 7.84% were sucked into the exhaust air cylinder and then emitted. The dusts with a diameter of 80 μm settled under the gravity effect, and showed uniform distribution.

(2) Distribution of dusts in vertical plane

Figure 19 shows the numbers of the cumulative dust particles with different diameters in vertical plane. It can be observed that, under single-forced condition, the dusts with diameters of 2.5 and 7 μm were slightly affected by gravity and showed no significant decrease in z value. For 20-μm dusts, less dusts were accumulated near the footway floor beyond a spreading distance of 30 m, suggesting that these dusts gradually settled. For the dusts with a diameter of 40 μm, the z value decreased obviously and the dusts mainly gathered below the forced air cylinder after a diffusion distance of 15 m. For the dusts with a diameter of 80 μm, the z value decreased rapidly at approximately 8 m away from the head-on section and the dusts finally accumulated within the range of 13 m away from the head-on section. Under single-exhaust condition, for the dusts with a diameter smaller than 20 μm, the z value increased and the dusts mainly gathered at the bottom of the footway 5 m away from the head-on section. By contrast, due to the gravity effect, the dusts with diameters of 40 and 80 μm mainly accumulated in the regions 5 and 3 m away from the head-on section, respectively.

(3) Diffusion velocity of the dusts

In order to compare the diffusion velocities of the dusts with different diameters under single-forced ventilation condition, the filled contour plot of the dust particle diameter, diffusion time, and the maximum diffusion distance was generated by means of first-order interpolation, as

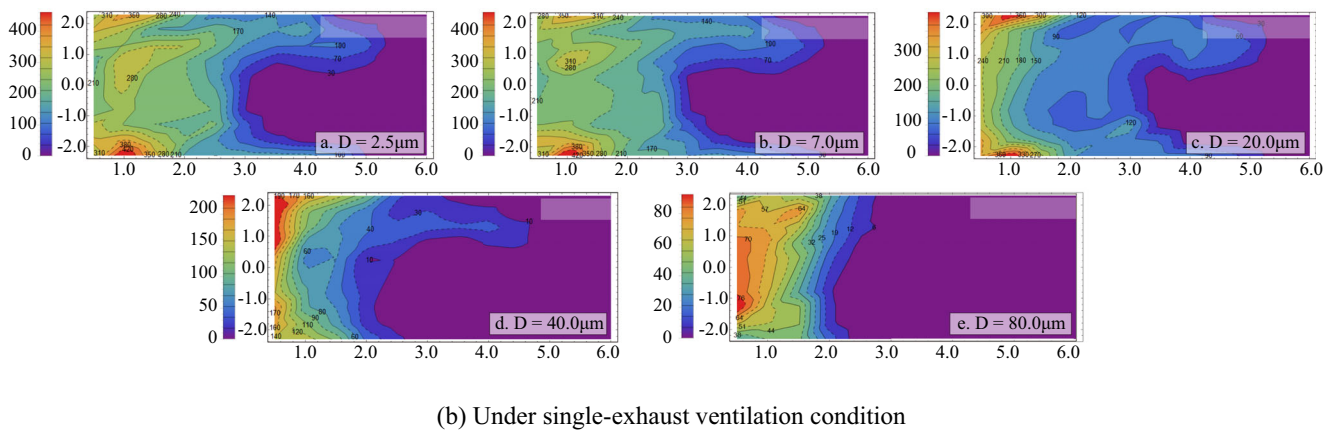
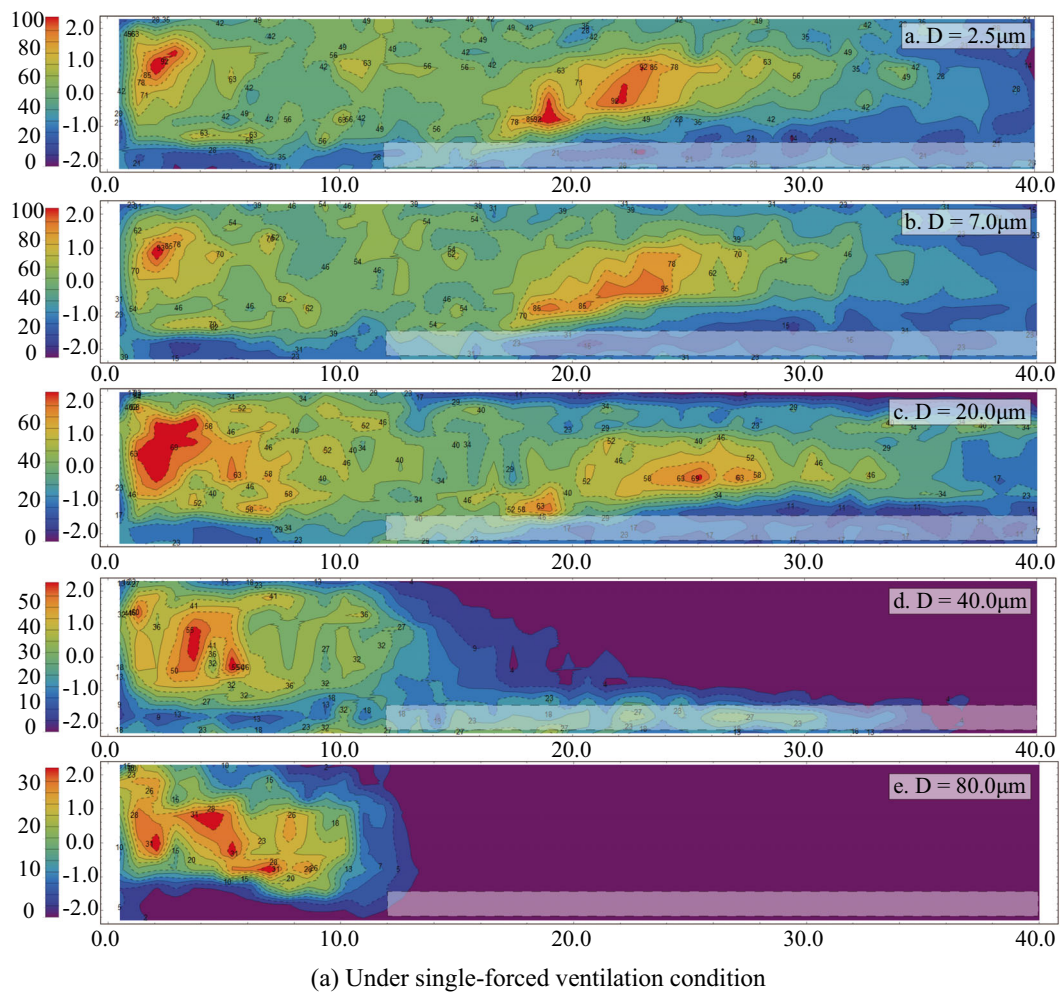


Fig. 18 Numbers of the cumulative dust particles with different diameters in horizontal plane, **a** under single-forced ventilation condition and **b** under single-exhaust ventilation condition

shown in Fig. 20. Under single-forced ventilation condition, the airflow intensity was strong around the head-on section, and the dusts with different diameters showed slight differences in diffusion velocity. With the increase of diffusion distance, the airflow intensity weakened, and the diffusion velocities of the great dust particles decreased

significantly. Additionally, with the increase of diffusion time, the maximum diffusion distances of the dusts with the diameter smaller than $40\ \mu\text{m}$ all increased, while the maximum diffusion distances of the dusts with the diameter over $40\ \mu\text{m}$ gradually stabilized.

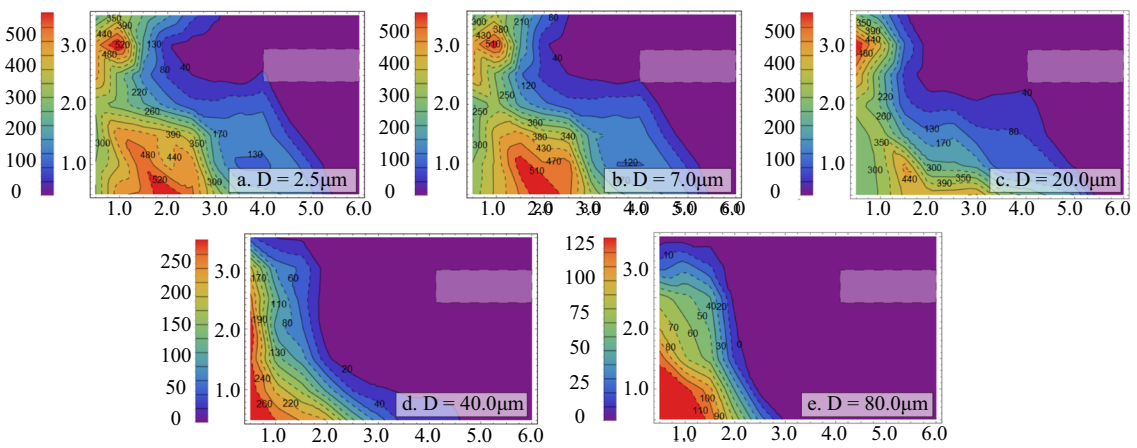
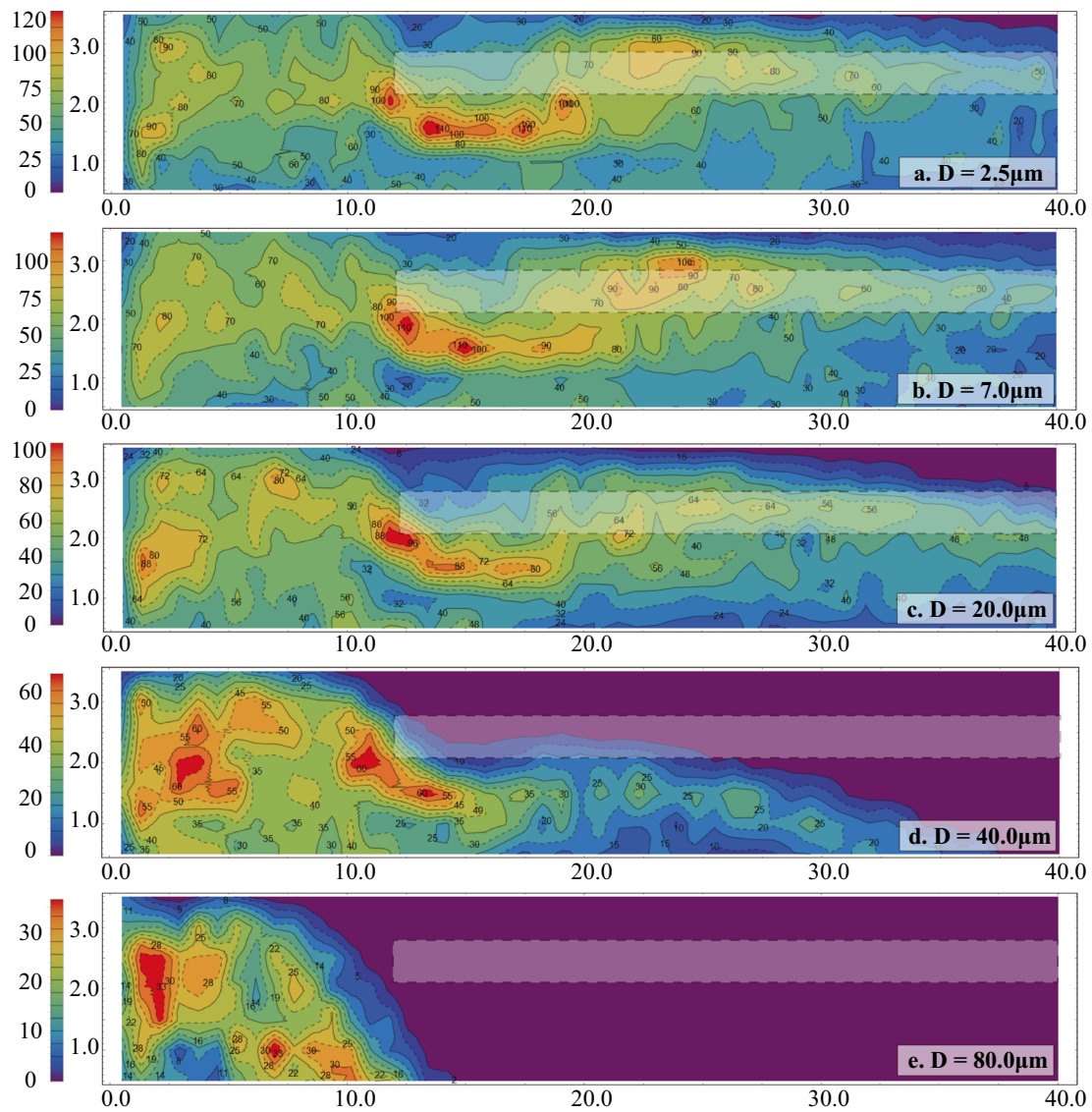


Fig. 19 Cumulative dust particles in vertical plane, **a** under single-forced ventilation condition and **b** under single-exhaust ventilation condition

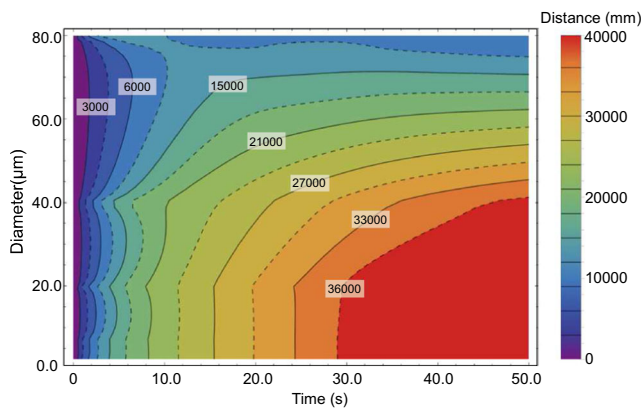


Fig. 20 Filled contour plot of the diffusion distance along the direction of y axis and diffusion time for the dusts with different diameters

Path-dependent settling behaviors of the dusts

The dusts showed fairly complex settling behaviors along the path, which were not only the results under the combined action of airflow drag force and gravity but also affected by the environmental conditions such as roughness and humidity of the footway walls (Goldasteh et al. 2013; Korevaar et al. 2014). In general, less dusts settled on the footway roof and both two sides, while the dusts tended to settle on the footway floor. In this study, the cumulative mass of the settled dusts in the different regions on the footway floor was acquired through EDEM post-processing, as shown in Fig. 21, in which the “Color Bar” denotes the cumulative mass of the settled dusts (different amounts of cumulative masses of the settled dusts were denoted by different colors in Color Bar). It can be observed that (1) under single-forced ventilation condition, the dusts with different diameters varied greatly in the path-dependent settling ratio (within a range of 15.29~100%). The greater the dust diameter is, the higher the path-dependent settling ratio is. Because of strong turbulence airflow around the head-on section and high-velocity airflow near the footway floor 10~20 m away from the head-on section, the dusts mainly settled around the head-on section and 10~20 m away from the head-on section. Moreover, the dusts with a diameter smaller than 7 μm are particularly harmful to human health, but their settling ratios were below 22.36%. This means that most of these dusts would pollute the working areas at the back of the footway. (2) Under single-exhaust ventilation condition, the dusts with different diameters mainly settled around the head-on section. The larger the dusts are, the higher the path-dependent settling ratio is. Moreover, the larger dusts also showed shorter path-dependent settling range. To be specific, the dusts with the diameter ranging from 2.5 to 20 μm mainly settled in the region 0~6 m away from the head-on section, while the dusts with diameters of 40 and 80 μm mainly settled in the regions 0~5 and 0~4 m away from the head-on section, respectively.

Conclusions

In this study, the airflow-dust coupled model in a blasting driving face was established using CFD-DEM coupled method. Moreover, the drag force, Magnus force, and Saffman force were applied in the model with the use of API interface to further improve the force characteristics of the dust particles. The relative errors between the field measured values of the dust field and the simulation results ranged from 0 to 17.82%, which verified the accuracy of the simulated airflow-dust coupled results.

- (1) Under single-forced ventilation condition, due to the action of the forced jet field, a vortex airflow field was formed in the region between the forced air outlet and the head-on section. The direction of airflows changed and pointed to the negative direction of y axis as the distance away from the head-on section increased. Under single-exhaust ventilation condition, the airflows between the footway end and the exhaust air inlet all pointed to the negative direction of y axis, and most airflows around the head-on region pointed towards the exhaust air inlet. In terms of dust suppression, the formed airflow field under single-exhaust ventilation condition is preferable.
- (2) Under single-forced ventilation condition, the motion trajectories of the dusts with the diameter smaller than 40 μm were close to the airflow line, and the dusts with different diameters generated vortex effects of varying degrees. Under single-exhaust ventilation condition, the motion trajectories of the dusts with the diameter smaller than 20 μm were close to the airflow streamline.
- (3) Under single-forced ventilation condition, a great number of dusts with the diameter smaller than 20 μm accumulated at locations 5 and 17~25 m away from the head-on section. With the increase of diffusion time, the maximum diffusion distances of the dusts with the diameter smaller than 40 μm all increased while the maximum diffusion distances of the dusts with the diameter over 40 μm reached stable values. Under single-exhaust ventilation condition, the dusts with the diameter smaller than 20 μm were distributed near the footway walls and the z values of the dusts at around the exhaust air inlet increased.
- (4) Under single-forced ventilation condition, the path-dependent settling behaviors of the dusts mainly occurred around the head-on section and at the location 10~20 m away from the head-on section; the dusts with a diameter smaller than 7 μm are particularly harmful to human health, but their settling ratios were below 22.36%. Under single-exhaust ventilation condition, the dust emission velocity decreased with the

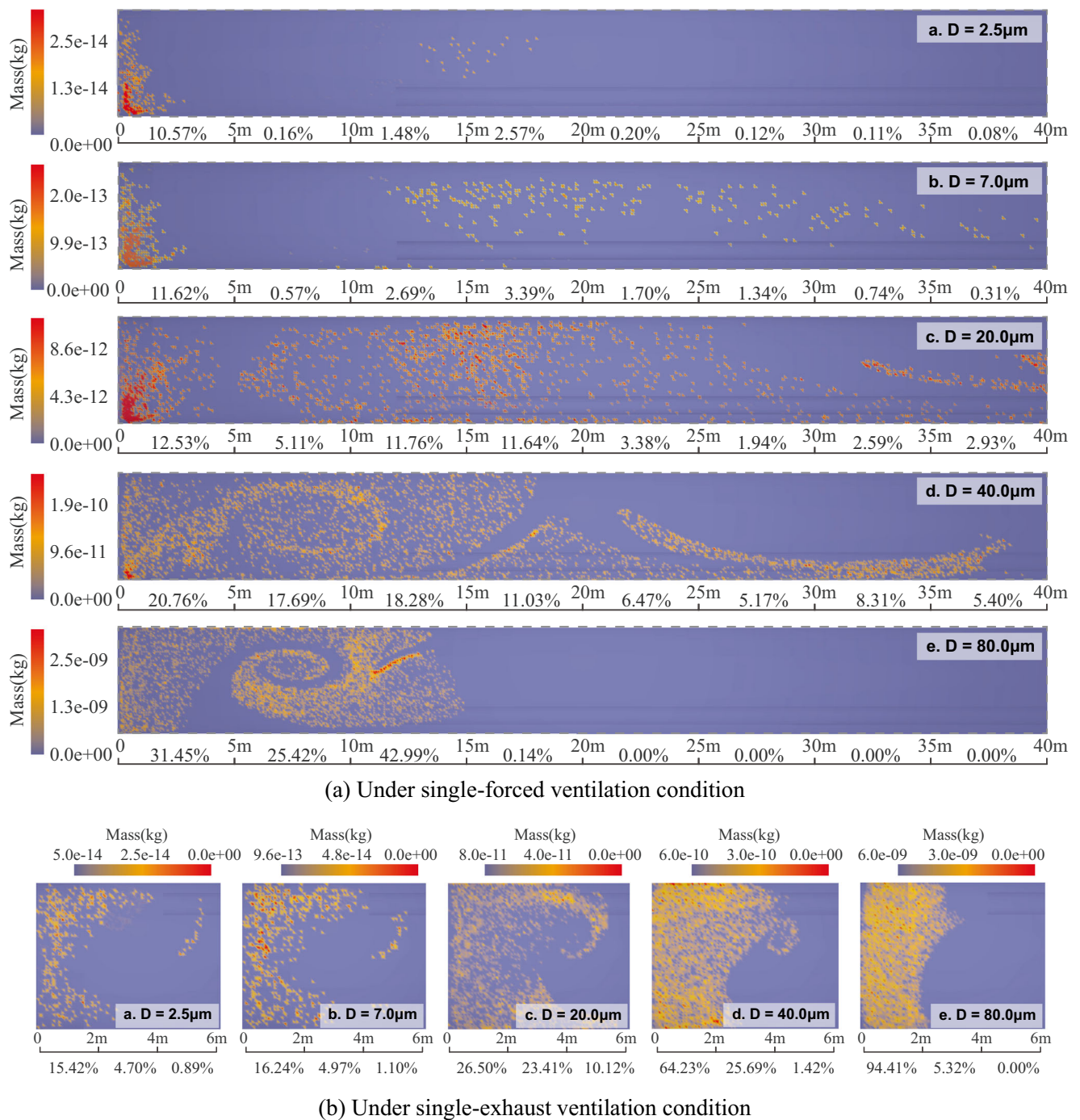


Fig. 21 Comparison between the path-dependent settling ratios among the dusts with different diameters, **a** under single-forced ventilation condition and **b** under single-exhaust ventilation condition

increase of diffusion time, and the emission ratios of larger dusts stabilized more quickly. Through nonlinear fitting, the relationship between dust diameter and negative-pressure-induced dust emission ratio can be expressed as $P = -25.03 \ln(D) + 110.39$; the dust emission ratio was up to 74.36% for 7- μm dusts. Moreover, the path-dependent settling behaviors of the dusts mainly occurred around the head-on section.

Overall, single-exhaust ventilation performed most favorable in dust control.

Acknowledgements This work was financially supported by State Key Program of National Natural Science of China (Grant No. U1261205), the Outstanding Youth Fund Project of Provincial Universities in Shandong Province (Grant No. ZR2017JL026), the Key Research and Development Program of Shandong Province (Grant No. 2016GSF120002), the Qingdao City Science and Technology Project (Grant No. 16-6-2-52-

nsh), and Sub Project of National Key Research and Development Program (Grant No. 2017YFC0805202).

References

- Akbarzadeh V, Hrymak AN (2016) Coupled CFD-DEM of particle-laden flows in a turning flow with a moving wall. *Comput Chem Eng* 86:184–191
- Akhshik S, Behzad M, Rajabi M (2015) CFD-DEM approach to investigate the effect of drill pipe rotation on cuttings transport behavior. *J Pet Sci Eng* 127:229–244
- Amritkar A, Deb S, Tafti D (2014) *Efficient parallel CFD-DEM simulations using OpenMP*. Academic Press Professional, Inc, Cambridge
- Chen M, Hu Y, Lu W et al (2011) Numerical simulation of blasting excavation induced damage to deep tunnel. *Rock Soil Mech* 32:1531–1537
- Chen J, Wang Y, Jiang Z (2013) Numerical simulation of blasting dust concentration distribution and diffusion regularities in stope. *J China Coal Soc* 38:147–152(6)
- Chen J, Wang Y, Li X et al (2015) Erosion prediction of liquid-particle two-phase flow in pipeline elbows via CFD-DEM coupling method. *Powder Technol* 275:182–187
- Erol I, Aydin H, Didari V, Ural S (2013) Pneumoconiosis and quartz content of respirable dusts in the coal mines in Zonguldak, Turkey. *Int J Coal Geol* 116–117:26–35
- Fan T, Zhou G, Wang J (2018) Preparation and characterization of a wetting-agglomeration-based hybrid coal dust suppressant. *Process Saf Environ Prot* 113:282–291
- Feng Y, Owen D (2014) Discrete element modelling of large scale particle systems—I: exact scaling laws. *Comput Part Mech* 1:159–168
- Goldasteh I, Ahmadi G, Ferro AR (2013) Monte Carlo simulation of micron size spherical particle removal and resuspension from substrate under fluid flows. *J Aerosol Sci* 66:62–71
- Habeeb L (2013) ANSYS 13.0 help, FLUENT theory guide
- Han Q, Yang N, Zhu J, Liu M (2015) Onset velocity of circulating fluidization and particle residence time distribution: a CFD-DEM study. *Particuology* 21:187–195
- Hertz H (1880) On the contact of elastic solids 92.
- Hu S, Wang Z, Feng G (2015) Temporal and spatial distribution of respirable dust after blasting of coal roadway driving faces: a case study. *Fortschr Mineral* 5:679–692
- Hu S, Feng G, Ren X et al (2016) Numerical study of gas–solid two-phase flow in a coal roadway after blasting. *Adv Powder Technol* 27:1607–1617
- Ji Y, Ren T, Peter W et al (2016) A comparative study of dust control practices in Chinese and Australian longwall coal mines. *Int J Min Sci Technol* 26:199–208
- Jiang Z, Chen M, Chen J (2013) Numerical simulation of dust concentration distribution and changing regularities in roadway stope blasting. *J Cent South Univ* 44:1190–1196
- Kim S, Jeong W, Jeong D, Seok J (2006) Numerical simulation of blasting at tunnel contour hole in jointed rock mass. *Tunn Undergr Space Technol Inc Trenchless Technol Res* 21:306–307
- Korevaar MW, Padding JT, Van Der Hoef MA, Kuipers JAM (2014) Integrated DEM-CFD modeling of the contact charging of pneumatically conveyed powders. *Powder Technol* 258:144–156
- Kurnia JC et al (2014) Dust dispersion and management in underground mining faces. *Int J Min Sci Technol* 24:39–44
- Nakayama S, Uchino K, Inoue M (1996) 3 dimensional flow measurement at heading face and application of CFD. *Shigen-to-Sozai* 112:638–644
- Nie W, Cheng WM, Bin YY et al (2012) The research and application on whole-rock mechanized excavation face of pressure ventilation air curtain closed dust removal system. *J China Coal Soc* 37:1165–1170(6)
- Nie W, Liu Y, Wei X, Hu X et al (2016a) Effect of suppressing dust by multi-direction whirling air curtain on fully mechanized mining face. *Int J Min Sci Technol* 26:629–635
- Nie W, Ma X, Cheng W et al (2016b) A novel spraying/negative-pressure secondary dust suppression device used in fully mechanized mining face: a case study. *Process Saf Environ Prot* 103:126–135
- Pandey SK, Tripathi BD, Mishra VK (2008) Dust deposition in a sub-tropical opencast coalmine area, India. *J Environ Manag* 86:132–138
- Petrov T, Wala AM, Huang G (2014) Parametric study of airflow separation phenomenon at face area during deep cut continuous mining. *Min Technol* 122:208–214
- Qin YP, Zhang MM, Cui LJ, Liu JY (2011) Numerical simulation of dust migration and study on dust removal modes with the forced ventilation shunt in a fully mechanized workplace. *J Univ Sci Technol Beijing* 33:790–794
- Ren YH, Qin YP (2013) Study on contraction of dust control system in continuous coal mining. *Adv Mater Res* 734-737:824–827
- Ren T, Wang Z, Cooper G (2014) CFD modelling of ventilation and dust flow behaviour above an underground bin and the design of an innovative dust mitigation system. *Tunn Undergr Space Technol* 41:241–254
- Sa Z, Li F, Qin B, Pan X (2012) Numerical simulation study of dust concentration distribution regularity in cavern stope. *Saf Sci* 50:857–860
- Shao T, Yinyu HU, Wang W et al (2013) Simulation of solid suspension in a stirred tank using CFD-DEM coupled approach. *Chin J Chem Eng* 21:1069–1081
- Toraño J, Torno S, Menéndez M, Gent M (2011) Auxiliary ventilation in mining roadways driven with roadheaders: validated CFD modelling of dust behaviour. *Tunn Undergr Space Technol Inc Trenchless Technol Res* 26:201–210
- Tsuji Y, Tanaka T, Ishida T (1992) Lagrangian numerical simulation of plug flow of cohesionless particles in a horizontal pipe. *Powder Technol* 71:239–250
- Wang (2011) Numerical simulation of dust distribution at a fully mechanized face under the isolation effect of an air curtain. *Int J Min Sci Technol* 21:65–69
- Wang Z, Ren T (2013) Investigation of airflow and respirable dust flow behaviour above an underground bin. *Powder Technol* 250:103–114
- Wang H, Wang D, Tang Y, Wang Q (2015a) Foaming agent self-suction properties of a jet-type foam preparation device used in mine dust suppression. *Process Saf Environ Prot* 98:231–238
- Wang Y, Luo G, Geng F et al (2015b) Numerical study on dust movement and dust distribution for hybrid ventilation system in a laneway of coal mine. *J Loss Prev Process Ind* 36:146–157
- Xie Y, Fan G, Dai J et al (2007) New respirable dust suppression systems for coal mines. *Int J Min Sci Technol* 17:321–325
- Zheng Y, Feng C, Jing G et al (2009) A statistical analysis of coal mine accidents caused by coal dust explosions in China. *J Loss Prev Process Ind* 22:528–532
- Zhou G, Qiu H, Zhang Q et al (2016a) Experimental investigation of coal dust wettability based on surface contact angle. *J Chem* 2016:1–8
- Zhou G, Zhang Q, Bai R, Ni G (2016b) Characterization of coal micro-pore structure and simulation on the seepage rules of low-pressure water based on CT scanning data. *Fortschr Mineral* 6:78
- Zhou G, Zhang Q, Bai R et al (2017) The diffusion behavior law of respirable dust at fully mechanized caving face in coal mine: CFD numerical simulation and engineering application[J]. *Process Saf Environ Prot* 106:117–128